AIAA Journal
Vol. 49, No. 8, August 2011

Space–Time Correlation Measurements in Near Fields of Jets

K. Viswanathan,* J. R. Underbrink,† and L. Brusniak‡
The Boeing Company, Seattle, Washington 98124

DOI: 10.2514/1.J050750

Space–time correlation characteristics of jets operated over a wide range of jet velocities are investigated in this study, in order to gain insights into the physical mechanisms that lead to generation and radiation of noise due to turbulent mixing in jets. A traversing semicircular cage array that spans 180° in the azimuthal direction and 30 diameters in the axial direction, together with four far-field microphone arrays at different azimuthal angles, are employed. Simultaneously sampled space–time data have been acquired, processed, and analyzed. Examination of the coherence spectra and correlations, with the reference microphone at different x/D locations, reveals the following: there is a large source region that is coherent over ∼15*D* axially and ∼360° azimuthally for heated and unheated jets in the Mach number range of 0.51 to 1.67; the coherent region typically extends from ∼13*D* to ∼30*D*, with maximum normalized correlation levels greater than ∼0.5 (50%) over the entire axial extent of ∼15*D*; and these high levels of normalized correlations are observed at all jet velocities. The near-field–far-field correlations again indicate an extended axial region of ∼15*D* where high correlations of ∼0.5 (50%) to ∼0.8 (80%) are observed between a single point in the near-field and far-field microphone signal at 150°, at all jet velocities. This large coherent region was completely missed in prior studies. The consistent trends from near-field and source measurements point to a single mechanism/source responsible for the generation and radiation of noise to the peak radiation sector.

I. Introduction

THE physical mechanisms that lead to generation and radiation of noise due to turbulent mixing in jets are not clearly understood. Complexities associated with the description of the time-dependent turbulence and the noise sources have proved to be extremely challenging. There have been several studies in the last three decades, using a variety of experimental and analytical techniques (see [1–8] for a short list of the earlier studies). The primary approach in many of these investigations is the measurement and the interpretation of the correlations of the fluctuating flow parameters within the jet, as well as the correlations of the flow fluctuations with the far-field noise. Important flow features and their distributions were identified. Advances in flow diagnostic instrumentation and experimental techniques have led to a resurgence of interest in gaining a better understanding of the fundamental mechanisms of turbulence-generated noise. There have been numerous studies in the last decade [9–36]. The salient results from these are summarized next.

Seasholtz et al. [9] developed and applied the Rayleigh scattering diagnostics to the measurement of velocity and density fluctuations in high-speed jets. Panda et al. [10,11] investigated the correlations of the density and velocity fluctuations at various axial locations along the jet centerline and the lip line with far-field pressure measurements at various polar angles. At supersonic convective Mach numbers, significant correlation was measured from the peripheral shear layer for far-field microphone angles greater than ∼130° (all polar angles are measured from the jet inlet axis); the correlations dropped at subsonic convective Mach numbers. However, significant correlations at low-Strouhal numbers were observed with the fluctuations along the jet centerline just downstream of the potential core, for unheated jets over a wide range of Mach numbers from 0.6 to 1.8 at large aft angles. There was virtually no correlation for any jet Mach number, when the microphone was located at 90°. These observations indicate that the region downstream of the potential core is a low-frequency sound source, with a noise generation mechanism very different from the Mach wave emission associated with supersonic convective velocities. Bridges et al. [12–14] carried out extensive surveys of the turbulence properties of subsonic and supersonic jets, with both conventional and dual particle image velocimetry (PIV) systems. Bridges and Wernet [14] extended their experimental technique for the measurement of time-resolved PIV of hot jets and examined the effect of heat addition on the distribution of turbulence statistics. The space–time correlations with the dual PIV system indicated that, for jets at fixed acoustic Mach numbers (V_j/a, in which a is the speed of sound in the external region, taken to be the ambient medium):

1) The addition of heat has a relatively small effect on the intensities of the turbulent kinetic energy, turbulence length, and time scales.

2) There is good collapse of the single-point and two-point statistics for cold and heated jets, if the streamwise location is normalized by the different lengths of the potential cores.

Fleury et al. [15] employed a dual PIV system, to quantify the space–time correlations in two isothermal subsonic jets, and found the following:

1) The length scales in the shear layer depend on the local momentum thickness for many of the correlations.

2) The space and time scales at large downstream distances are close to the values expected in homogeneous and isotropic turbulence.

In another study at NASA John H. Glenn Research Center at Lewis Field, the hydrodynamic pressure fields of subsonic jets were measured with six circular arrays (see Suzuki and Colonius [16]). The arrays extended to a downstream distance of ∼8*D*, with a half-cone angle of 11.3°. The radial extent of the microphones was in the range of 1*D* to 1.75*D* at $x/D = 2.25$. Suzuki and Colonius examined the evolution and the modal content of the instability waves in the initial mixing layer and their relation to far-field noise. Arndt et al. [18] used the proper orthogonal decomposition technique to deduce the large-scale structures from pressure measurements in the hydrodynamic field.

There have also been focused programs on source diagnostics at the United Technology Research Center (UTRC) [19–22], the Ohio

---

Presented as Paper 2010-3784 at the 16th AIAA/CEAS Aeroacoustics Conference, Stockholm, Sweden, 7–9 June 2010; received 3 July 2010; revision received 6 March 2011; accepted for publication 15 March 2011.

*Boeing Technical Fellow, MS 67-ML, Post Office Box 3707; k.viswanathan@boeing.com. Associate Fellow AIAA.

†Boeing Technical Fellow, MS 67-ML, Post Office Box 3707; james.r.underbrink@boeing.com. Senior Member AIAA.

‡Aeroacoustics Engineer, MS 67-ML, Post Office Box 3707; leon.brusniak@boeing.com. Member AIAA.

State University [23,24], the University of Poitiers [25–30], and the Pennsylvania State University [31–33]. A rotating array was used to map the space–time correlations in the near field of a transonic and a supersonic jet in the UTRC experiments. Two linear conical arrays of 8 (or 11) microphones with a half-angle of 7° and an axial spacing of $1.25D$ were employed; the axial extent of the arrays was $10D$ (or $14D$). The radial distance of the microphones spanned a range of $0.97D$ closest to the nozzle exit and $2.5D$ for the most downstream microphone. The pressure fields in this hydrodynamic region are dominated by those associated with the large-scale turbulence structures. They showed that the near-field pressure statistics were well represented by a Gaussian wave-packet model for both the subsonic and supersonic jets. Reba et al. [21] modeled the noise radiated by the large-scale turbulence as a wave packet, with an equivalent source given by the two-point space–time correlation of the pressure measured on the conical surface surrounding the jet. The near-field pressure was extended to the far field through the use of a

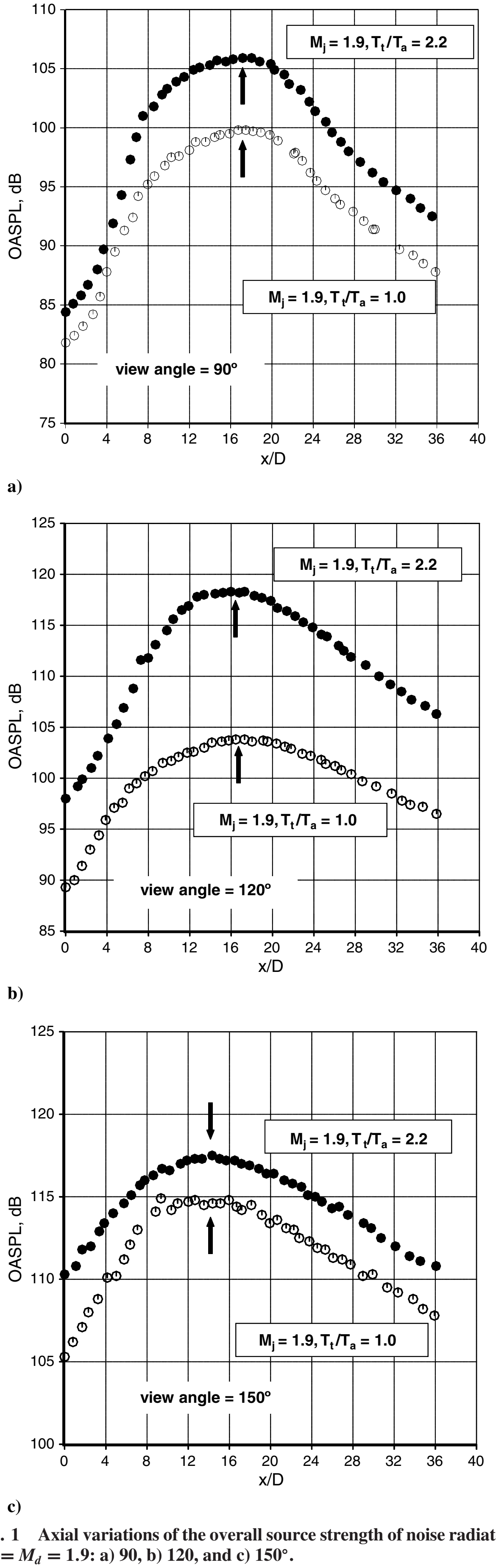

Fig. 1 Axial variations of the overall source strength of noise radiated, $M_j = M_d = 1.9$: a) 90, b) 120, and c) 150°.

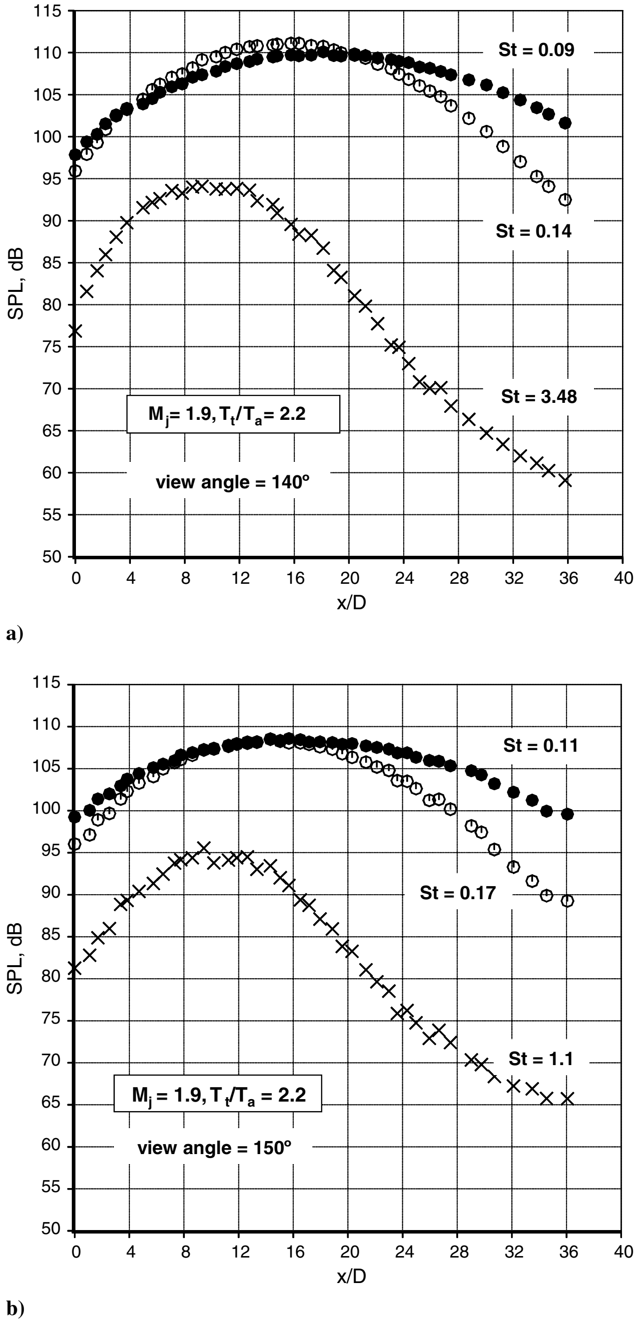

Fig. 2 Axial variations of the noise radiated at selected frequencies, $M_j = M_d = 1.9$ and $T_t/T_a = 2.2$: a) 140 and b) 150°.

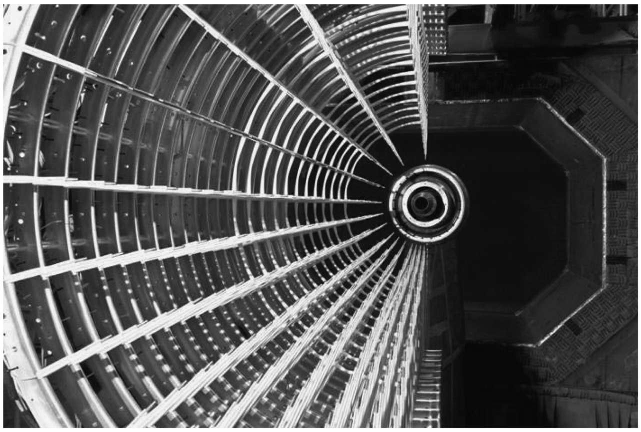

Fig. 3 Photograph of the cage array taken from downstream direction. The microphones are concentric with the jet axis.

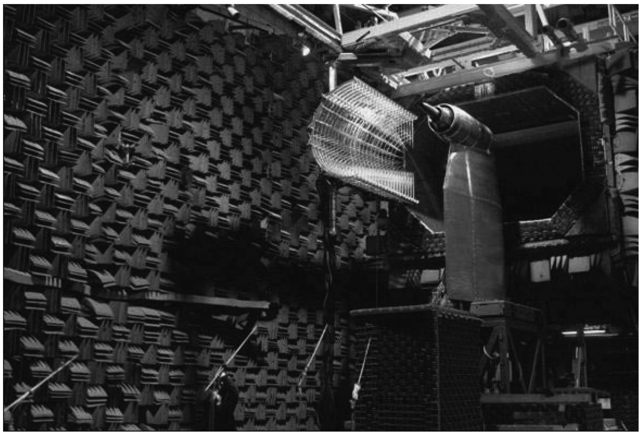

Fig. 4 Photograph of the cage array located laterally away from the jet.

Green's function. The role of the large-scale structures in the generation of noise to the peak angles was established with this approach.

In the research reported in [23,24], the focus was on linking the events in the instantaneous development and evolution of the large turbulence structures in the jet with the far-field acoustics. Both near-field and far-field microphones were used in conjunction with laser diagnostics of the flowfield. The measurements indicated a strong connection between the dynamics of the large-scale structures and the noise radiated to large aft angles. The studies at the University of Poitiers [25–30] sought to relate the dynamics of the flow with radiated noise to all radiation angles via the simultaneous measurement of the pressure and velocity fields in the vortical flow and the pressure fields in the near field and far field. Through a filtering of the near pressure field and stochastic analysis of the measured parameters, certain relations between the flow characteristics and the far-field spectra were formulated. They employed a linear array with a half-cone angle of 9° and an axial extent of $11D$. The axial spacing was $0.2D$ closer to the nozzle exit and $0.4D$ further downstream; the radial distance was $0.8D$ at the nozzle exit plane. A wave number analysis was employed to delineate between the hydrodynamic and acoustic fields.

The technique of optical deflectometry was used to measure space–time correlations in circular and beveled nozzles in [31,32]; both subsonic and supersonic jets were considered. In an extension of this technique, Papamoschou et al. [33] used four optical deflectometry probes simultaneously with a far-field circular array of eight microphones in the peak noise radiation direction of a cold $M = 1.75$ jet. The probes were placed both inside the flow and at varying radial distances outside the jet. The beam-formed signals from both the probes and the microphones were correlated, so as to enhance the coherence between the flow and the noise radiated to the peak radiation angle. When the probes were traversed in the radial direction, the levels of correlation with the far-field noise initially dropped in the hydrodynamic field and then increased to significant levels in the acoustic field. Bogey et al. [34] examined the spectral characteristics of the near-field and far-field spectra of subsonic jets. Finally, Gutmark and his coworkers (see Callender et al. [35] and Kastner et al. [36]) have also examined the near-field pressure contours of various nozzle geometries. It is emphasized that this list of references is a representative sample of the different studies but is by no means comprehensive.

Before we describe the current program, it is worthwhile to examine the source distributions obtained with an elliptic mirror so as to set the stage for what is to follow. This is a short summary of the results reported recently by Viswanathan [37]. The apparent sources were measured by an elliptic mirror with an aperture of 1.5 m, which could be traversed in the axial direction as well as swiveled to map the axial source distribution to any desired radiation angle. The resolution limit at the lower frequency for the mirror is ~1500 Hz. The jet considered here has a Mach number of 1.9. A convergent–divergent (CD) nozzle of exit diameter of 1.27 in. (3.23 cm) was operated at the design Mach number. A small nozzle diameter was specifically chosen to drive the peak frequencies to higher values, so that the lower-frequency limit for the resolution of the elliptic mirror does not affect the measurements at frequencies of interest. Figures 1a–1c show the axial variation of the overall sound pressure level (OASPL) of the sources for the Mach number $M_j = 1.9$ jet at two stagnation temperature ratios of 1.0 and 2.2. The polar radiation or viewing angles of the elliptic mirror are 90, 120, and 150°, respectively. Similar plots at intermediate angles of 110, 130, and 140° are shown in Fig. 2 in Viswanathan [37]. The peak source locations, highlighted by arrows, are broad and located in the vicinity of ~$17D$ for the angular range of 90 to 120° for the unheated and

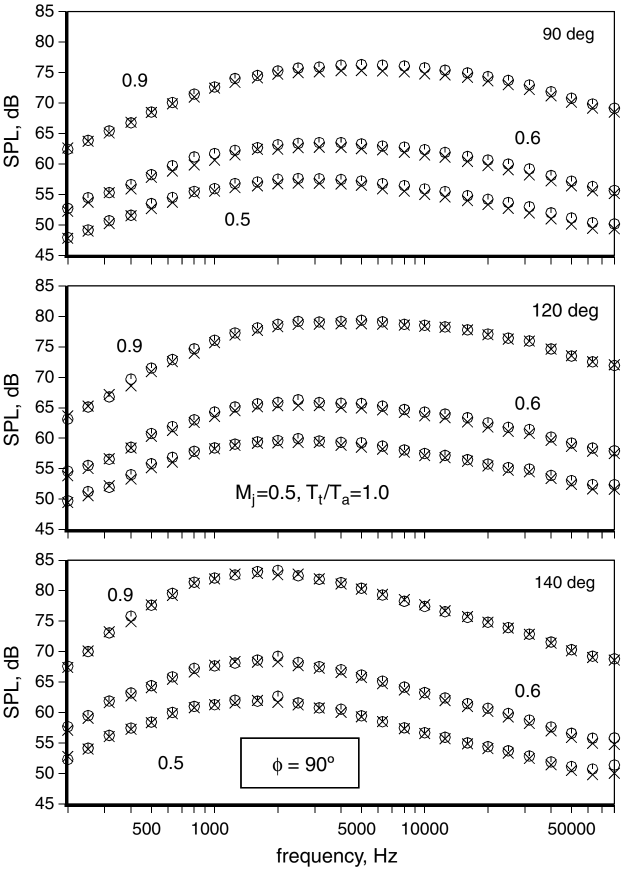

Fig. 5 Spectral comparisons at different polar angles, $\phi = 90°$. Unheated jets with $M_j = 0.5, 0.6$, and 0.9. o: before array installation. x: with array in position 1.

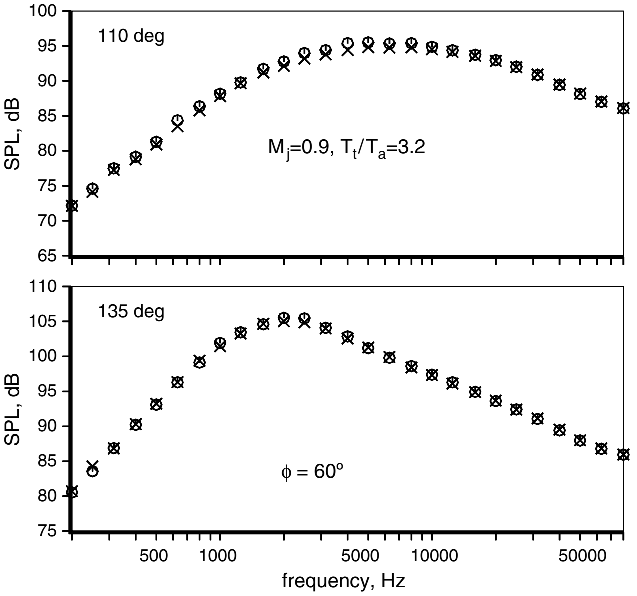

Fig. 6 Spectral comparisons at different polar angles, $M_j = 0.9$ and $T_t/T_a = 3.2$: $\phi = 60°$ (left) and $\phi = 30°$ (right). o: before array installation. x: with array in position 1.

heated jets. For larger aft angles, the peaks shift slightly closer to the nozzle and are located at $\sim 15D$.

Figures 2a and 2b show the axial distribution of noise radiated at selected individual Strouhal numbers. The radiation angle is 140° in Fig. 2a, and the Strouhal numbers are 0.09, 1.4, and 3.28; the corresponding raw frequencies are 2000, 3150, and 80,000 Hz, respectively. The radiation angle is 150° in Fig. 2b, and the Strouhal numbers are 0.11, 0.17, and 1.1; the corresponding raw frequencies are 2500, 4000, and 25,000 Hz, respectively. Note that these frequencies are greater than the lower-resolution limit for the mirror. For the noise radiated to 140°, the peak locations for these frequencies are at $\sim 20D$, $\sim 16D$, and $\sim 10D$. Similarly, the peak locations at 150° are at $\sim 18D$, $\sim 16D$, and $\sim 10D$. Obviously, the peaks for the higher-Strouhal numbers move closer to the nozzle exit. Similar trends are observed for the unheated jet. The potential core length for this jet Mach number is $\sim 8D$ to $\sim 9D$. Clearly, the peak sources in Fig. 1 are located approximately two potential core lengths downstream from the nozzle exit. The more important observation is the following: at the lower frequencies, the length of the source region is quite long and spans $\sim 20D$ in the axial direction. That is, the sources for the lower frequencies are definitely not localized but extend over a considerable axial length.

This summary brings us to the current investigation. The true sources of jet noise are not uniquely identified to date, though there have been many descriptions. The objective of this investigation is the attainment of better understanding of the source characteristics, through the measurements of near-field space–time correlations. Implicit in this approach is the assumption that the features of the true sources will be imprinted on the near-field pressure correlations. Therefore, the interpretations of the results are based on "equivalent" sources. Though the term *source* is used throughout the paper, it specifically refers to "equivalent source" and should be taken as such. The main features of the experimental program are described in Sec. II. Four types of results, viz., 1) near-field space–time

Table 1 Test matrix for near-field measurements

Nozzle pressure ratio	T_t/T_a	M_j	V_j/a	M_c
Convergent nozzle				
1.21	1.0	0.52	0.51	0.36
1.28	1.0	0.60	0.58	0.41
1.69	1.0	0.90	0.83	0.58
3.00	1.0	1.36	1.16	0.81
4.65	1.0	1.66	1.33	0.93
1.21	3.2	0.53	0.91	0.64
1.69	3.2	0.91	1.50	1.05
3.00	3.2	1.37	2.10	1.47
4.65	3.2	1.67	2.42	1.69
CD nozzle ($M_d = 1.67$)				
3.00	1.0	1.36	1.16	0.81
4.65	1.0	1.66	1.33	0.93
3.00	3.2	1.37	2.10	1.47
4.65	3.2	1.67	2.42	1.69

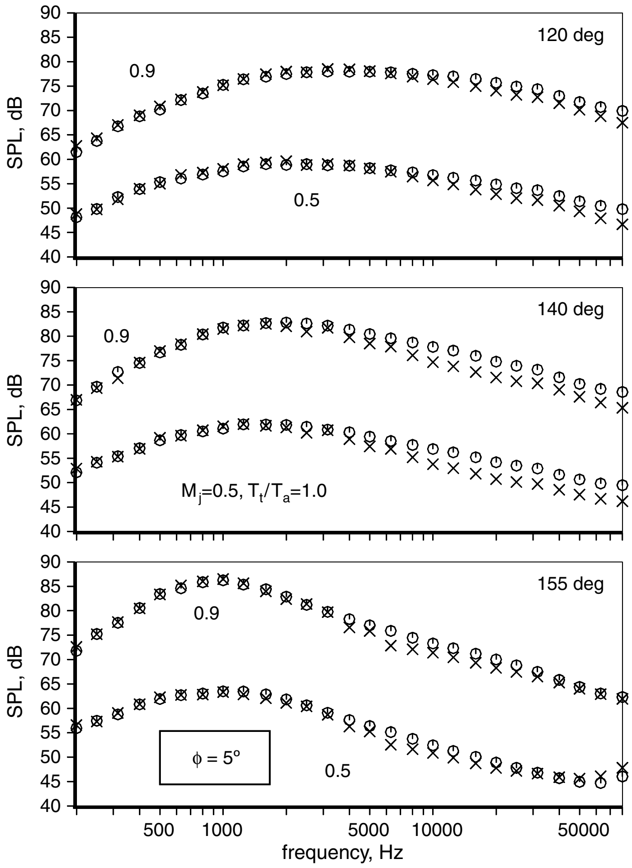

Fig. 7 Spectral comparisons at different polar angles, $\phi = 5°$. Unheated jets with $M_j = 0.5$ and 0.9. o: before array installation. x: with array in position 1.

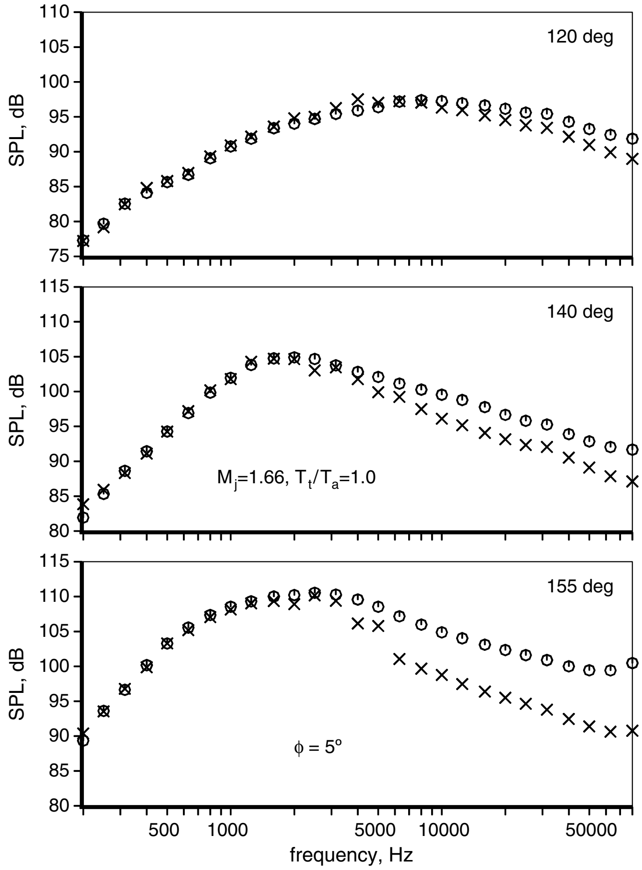

Fig. 8 **Spectral comparisons at different polar angles, $\phi = 5°$, $M_j = 1.66$ and $T_t/T_a = 1.0$. o: before array installation. x: with array in position 1.**

characteristics, 2) near-field–far-field correlations, 3) near-field mapping of pressure, and 4) far-field–far-field correlations, along with discussions, are presented in Sec. III. The main conclusions are summarized in Sec. IV. This paper is focused on the experimental technique, the test conditions, and the presentation/interpretation of data. The use of the measured data in developing and validating a theory for extending the near-field pressure to far-field spectra is covered in two companion papers [38,39].

II. Experimental Program

The experimental measurements were carried out in the Boeing Low-Speed Aeroacoustics Facility. Descriptions of the anechoic facility, the jet simulator, the capabilities of the jet simulator and the freejet wind tunnel, the facility-dedicated data acquisition systems, and other details are provided in Viswanathan [40–42]. Two different nozzles, a convergent nozzle and a CD nozzle, both with the same exit diameter of 2.45°, are used. The characteristics of only the turbulent mixing noise are considered in this paper.

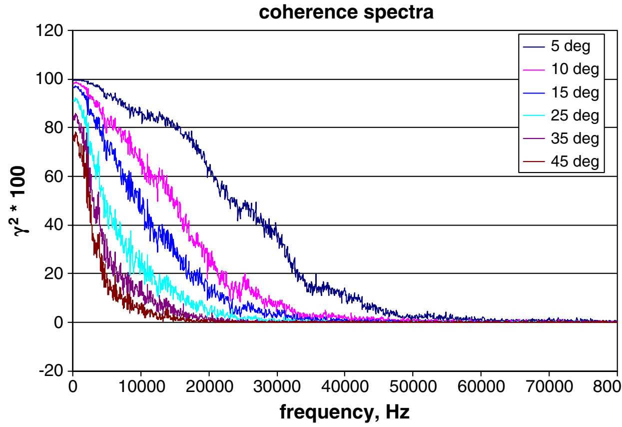

Fig. 9 **Azimuthal coherence, $M_j = M_d = 1.67$ and $T_t/T_a = 1.0$. Reference microphone at $x/D = 10.0$ and $\phi = 0°$. The second microphone is located at $x/D = 10.0$; ϕ varies from 5 to 45°.**

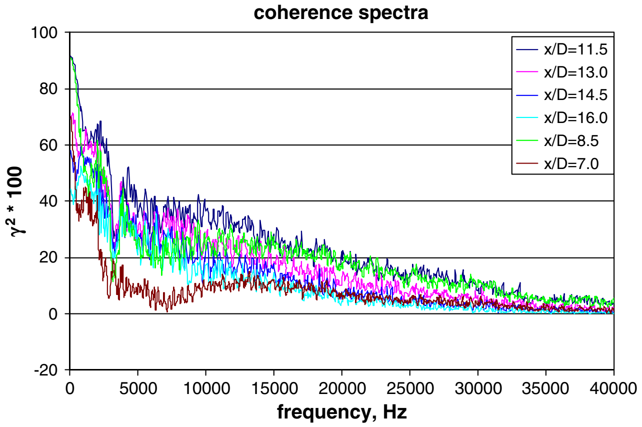

Fig. 10 **Axial coherence, $M_j = M_d = 1.67$ and $T_t/T_a = 1.0$. Reference microphone is at $x/D = 10.0$ and $\phi = 0°$. The second microphone is located at $\phi = 0°$; x/D varies from $x/D = 7.0$ to 16.0.**

A. Description of Microphone Arrays

For this particular test, a near-field conical cage array is designed and constructed. The half-angle of the cone is 10°. There are 21

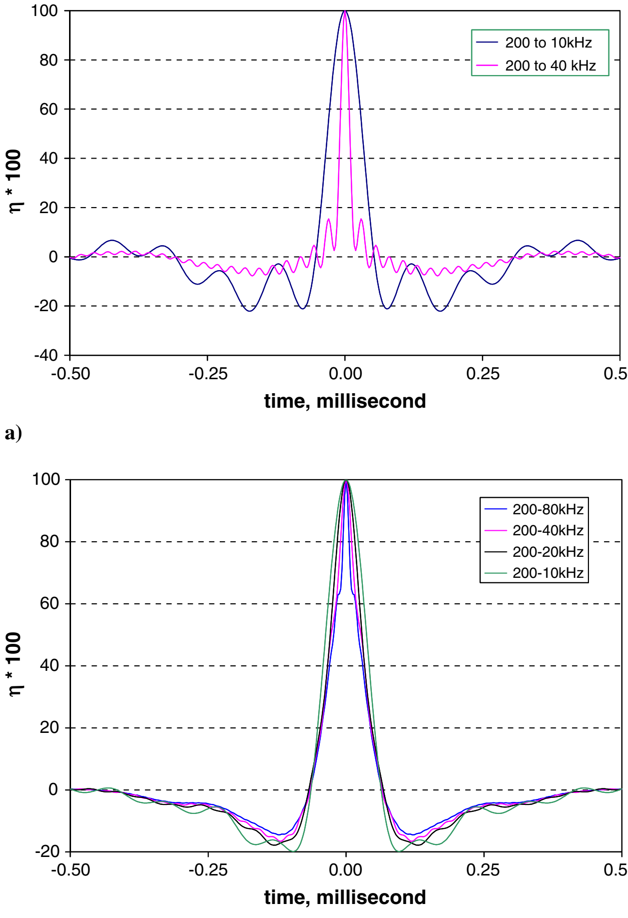

Fig. 11 **Effect of bandwidth on autocorrelation function, $M_j = M_d = 1.67$ and $T_t/T_a = 1.0$: a) microphone at $x/D = 7.0$ and $\phi = 0°$ and b) microphone at $x/D = 13.0$ and $\phi = 0°$.**

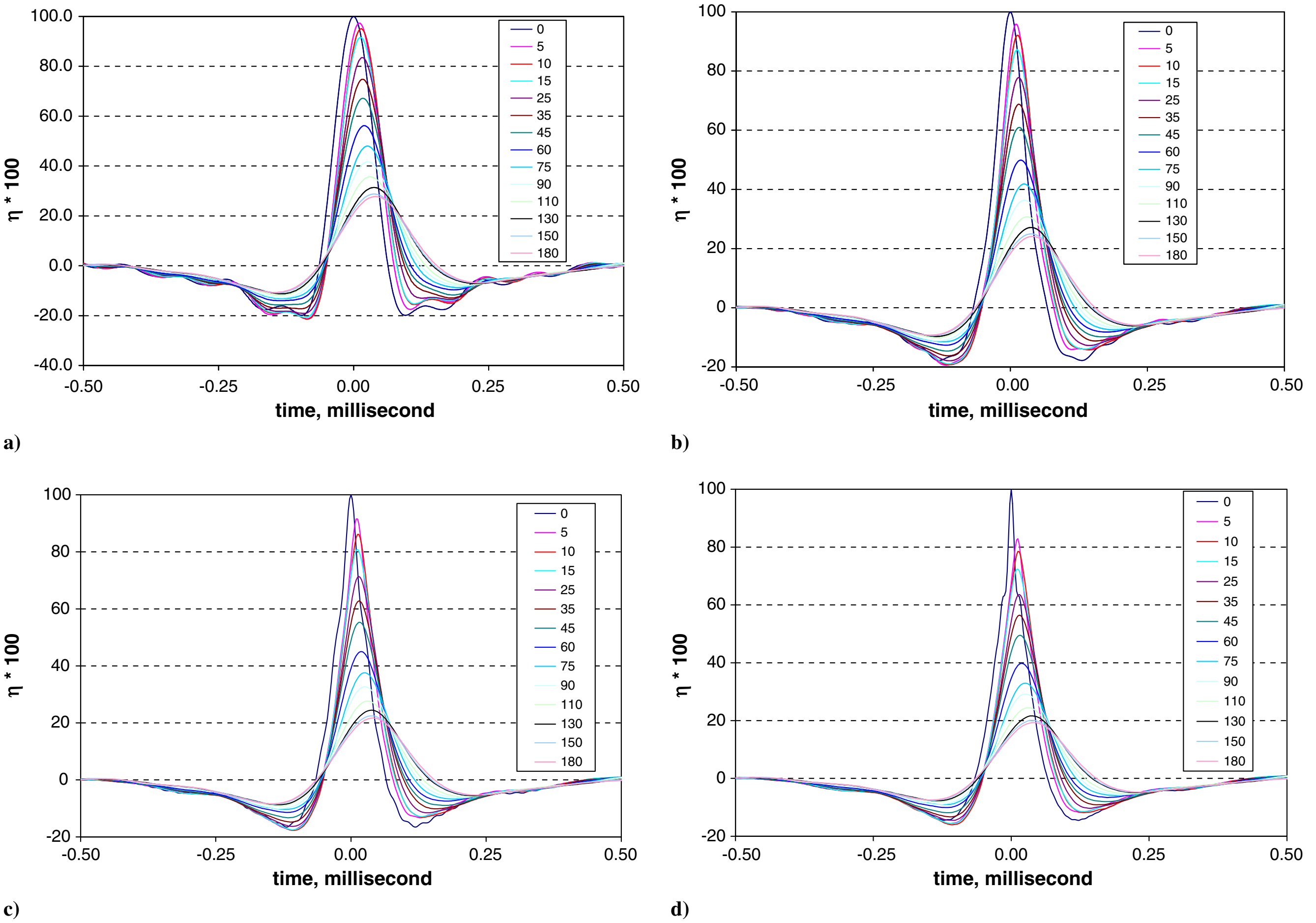

Fig. 12 Effect of bandwidth on cross-correlation function, $M_j = M_d = 1.67$ and $T_t/T_a = 1.0$. Reference microphone at $x/D = 13.0$ and $\phi = 0°$; second microphone at $x/D = 13.0$ and $\phi = 0$ to 180°: a) 200 Hz to 10 kHz, b) 200 Hz to 20 kHz, c) 200 Hz to 40 kHz, and d) 200 Hz to 80 kHz.

semicircular rings, with 14 microphones at various azimuthal angles in each ring, for a total of 294 near-field microphones. Figure 3 shows a photograph of the cage array, viewed from the downstream direction; the cascaded rings of microphone diaphragms forming a conical surface are highlighted in this view. The microphones are concentric with the jet axis in this array location. The desire to measure the near-field and far-field pressures simultaneously dictated the choice of semicircular rings; this arrangement, with the far-field array located on the opposite side of the near-field array, allowed a direct line of sight to the far-field microphones by not blocking the acoustic ray path. The following convention is used for defining the azimuthal angles ϕ: 0° corresponds to the bottom dead center (toward the ground), and the angle is measured counterclockwise. Each azimuthal ring spans 180°, from 180 to 360° (or 0°). The azimuthal spacing is as follows; for the sake of easy comprehension, the azimuthal positions are given with the angles measured in the clockwise direction (there should be no confusion, as these angles are obtained by subtracting from 360°), starting from the bottom dead center: 0, 5, 10, 15, 25, 35, 45, 60, 75, 90, 110, 130, 150, and 180 deg. As seen, the azimuthal spacing starts at 5° initially and incrementally increases to 10, 15, 20, and finally to 30° between the last two microphones. The axial spacing between the rings is uniform and is 1.5*D* for this particular test. Figures 1 and 2 provide critical information as to the requirements of the array length: the axial extent of the array, the distance between the first and the last rings, is chosen to be 30*D* (6.125 ft in length), based on the length of the low-frequency source observed in Fig. 2.

Several design features are incorporated in the array design, so that there is flexibility and ability to easily modify the array layout including the cone half-angle, axial positions of the rings, and circumferential positioning of the microphones at various desired azimuthal locations within each ring. These design features allow for tailoring of any of these geometric parameters for specific applications in future tests. The array, with all the instrumentation and the associated cables, needs to have adequate structure for cage strength and rigidity, while achieving as much acoustic transparency as possible so that far-field microphone data will not be affected by scattering off the array structure. Lack of interference is achieved by presenting a “thin” and “soft” profile to the jet noise sources: the structural profile is narrow, and there are no flat surfaces or sharp corners, as the cage is viewed from the location of a jet source. Structural strength is achieved by incorporating depth into the structural elements (rings and ring interconnecting pieces). Even though deep structural elements create large flat reflective surfaces relative to the acoustic wavelengths of interest, these surfaces are oriented relative to the jet noise surfaces such that the reflected sound will pass through the array structure in a direction opposite the far-field microphones. Cables are run on the back edges of the array structural elements, effectively “hiding” them from the viewpoint of the sound sources. This arrangement of cables is also critical to providing a noncontaminating measurement apparatus. The cage is attached to an overhead strut, which itself is attached to a mechanism that enables traversing the entire array in a plane horizontal to the ground.

The axis of the cage array is first aligned with the jet axis, so as to maintain concentricity of the microphones. Once the height of the array is fixed at the proper position (z-direction), the entire array can be moved in the x-y plane. The radial distance of the microphones to the jet axis can be controlled by moving the array in the axial direction. The array can be moved in the lateral direction (y-direction) so as to map the pressure field on a cross-sectional plane, using the microphones located at an azimuthal angle of 270°. Figure 4 shows a photograph of the array at a lateral location, different from that shown in Fig. 3, away from the jet. The array could also be stowed, further away from the jet than shown in Fig. 4 and more forward of the jet exit, when far-field data alone were acquired. Given the large size of the array in close proximity to the jet, it is imperative to minimize potential reflections from the array components. Again, several design features are incorporated to produce a lower profile, with soft/rounded corners for the cage structure and a well-thought-out strategy for hiding the 294 cables behind the strut. All of these prudent steps resulted in an “acoustically noninterfering” or “minimally reflective” array design, as will be demonstrated in the next section.

Four different far-field microphone arrays are deployed; these are at azimuthal angles of 90, 60, 30, and 5°, respectively. These four arrays are on the opposite side of the jet from the cage array (which subtends azimuthal angles from 180 to 360°). There are 14 microphones at polar angles of 50, 60, 70, 80, 90, 100, 110, 120, 125, 130, 135, 140, 145, and 150 deg for the arrays at azimuthal angles of 90, 60, and 30°. There are six microphones at polar angles of 110, 120, 130, 140, 150, and 155 deg for the array at an azimuthal angle of 5°. The 90° azimuthal array is at a constant polar radius of 25 ft (7.62 m) from the origin of the coordinate system, located on the jet axis at the nozzle exit plane. The 60 and 30° azimuthal arrays are at a constant linear sideline distance of 15 ft (4.57 m) parallel to the jet axis. The slant distances to the 5° microphone varied from 11.5 ft (3.5 m) to 24.8 ft (7.56 m). There are 48 microphones in the far field, in addition to the 294 on the cage array, for a total of 342 microphones.

B. Data System and Acquisition

For the near-field cage array measurements, Brüel and Kjaer type 4938-W-001 quarter-inch microphones are used with Brüel and Kjaer type 2670-W-001 preamplifiers. For the far-field measurements, Brüel and Kjaer type 4939 quarter-inch microphones are used with Brüel and Kjaer type 2670-W-001 preamplifiers. Dual-purpose power supplies custom-built by Boeing are used to power and condition the analog signals for all 342 microphones. Identical cables with matched lengths are used for all the array microphones, so as to eliminate any differences in the line responses that might impact the acquired data.

Boeing’s distributed digital data system 2 (DDS2) is used to acquire the acoustic data from the cage array and the far-field polar arrays. DDS2 is a data acquisition system built from National Instruments data acquisition PXI hardware and custom Boeing software. The system architecture [43,44] provides inherent channel-to-channel phase matching of better than ±0.5 deg up to 92.8 kHz. Data are sampled from all 342 microphones simultaneously at 204.8 kHz samples per second for each channel. Time-series data are acquired for 16 contiguous seconds, and time-series files are archived so as to retain maximum flexibility in postprocessing of the data.

The microphones are installed without the grid cap, so as not to compromise the ability to measure pressure signals above a frequency of ~40 kHz. In general, the accuracy of the measurements is within ±0.5 dB. Custom-built electronics serves to minimize the magnitude of the corrections that need to be applied to as-measured raw spectra: the resulting magnitude of the corrections is less than 0.1 dB up to a frequency of 10 kHz and is less than 1 dB for the frequency range of 10–40 kHz. For higher frequencies, the corrections are ~1.8 dB. As will be shown later, there is virtually no coherence above ~40 kHz; the implication is that the magnitude of the corrections is less than 1 dB for the frequencies of interest. Given the distributed sources for the near-field measurements, it was decided not to apply any corrections (free-field or random incidence, for example) to the cage array signals. However, the expected performance of the cage array instrumentation was validated by placing a speaker at a known location and ensonifying the cage array with white noise. Analysis of the data from this exercise indicated that the instrumentation properly characterizes the expected acoustic propagation phenomena; the fidelity of the instrumentation system was thus verified.

C. Test Matrix

As already noted, a convergent nozzle and a CD nozzle with a design Mach number of 1.67 are used. Both of them had the same exit diameter of 2.45 in., so as to maintain consistency in spacing, etc., for the cage array. Unheated jets and heated jets at a stagnation temperature ratio (T_t/T_a) of 3.2 over a wide range of jet Mach numbers from 0.51 to 1.67 have been considered. The convective Mach number M_c, taken to be $0.7(V_j/a)$, spans a range of 0.36 to 1.69. Recently, Viswanathan [45,46] offered the following experimental evidence:

1) The spectra at angles close to the jet axis attain the same large-scale similarity shape, regardless of the jet velocity.

2) There is a gradual transition from a broad (fine-scale similarity) spectra to a peaky spectra with rapid dropoff in the spectral levels away from the peak.

3) The azimuthal coherence of the far-field spectra is maintained at high levels, ≥ 0.54, even for microphones separated by 150° for low-velocity jets with $V_j/a = 0.4$.

With these results, Viswanathan [45,46] made the case that a single source or mechanism associated with the large-scale turbulence structures/instability waves is responsible for the radiation of noise to large aft angles, regardless of jet velocity.

Measurements in the current test over a wide range of convective Mach numbers, from 0.36 to 1.69, allow for investigation of the suggested mechanism. The test matrix is shown in Table 1. At each jet condition, both near-field and far-field measurements were made simultaneously at several array positions, as follows:

1) The radial distance at the nozzle exit plane ($x/D = 0.0$) for the conical surface formed by the diaphragms of the cage microphones is $3D$ from the jet centerline, and the cage array spanned a distance of $1D$ to $31D$.

2) The radial distance at $x/D = 0.0$ is $3.53D$ from the jet centerline, and the cage array spanned a distance of $-2D$ to $28D$.

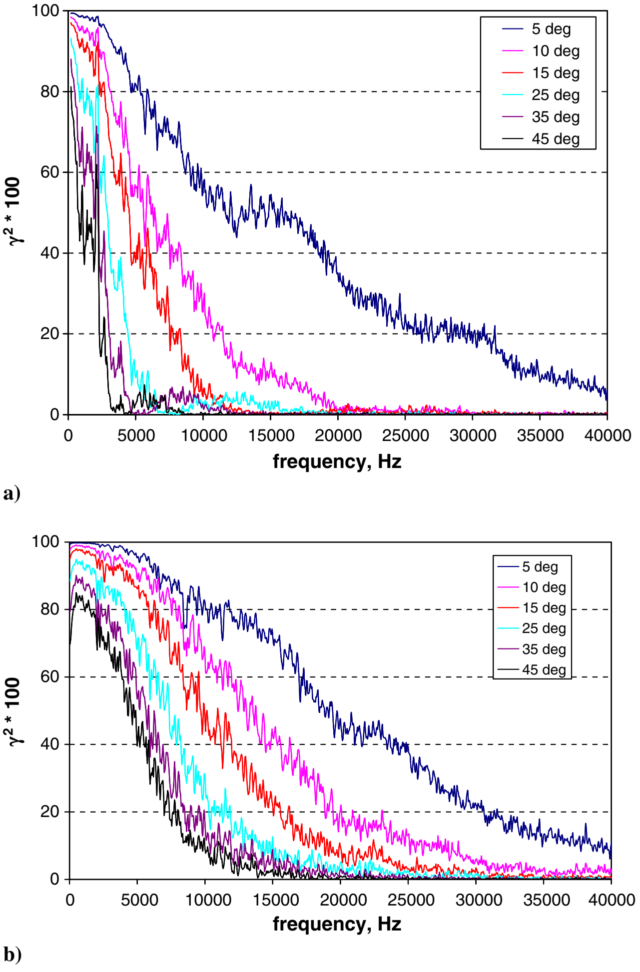

Fig. 13 Azimuthal coherence, $M_j = M_d = 1.67$ and $T_t/T_a = 1.0$. Reference microphone at a) $x/D = 4.0$ and $\phi = 0°$ and b) $x/D = 16.0$ and $\phi = 0°$. The second microphone is located at a) $x/D = 4.0$ and b) $x/D = 16.0$; ϕ varies from 5 to 45°.

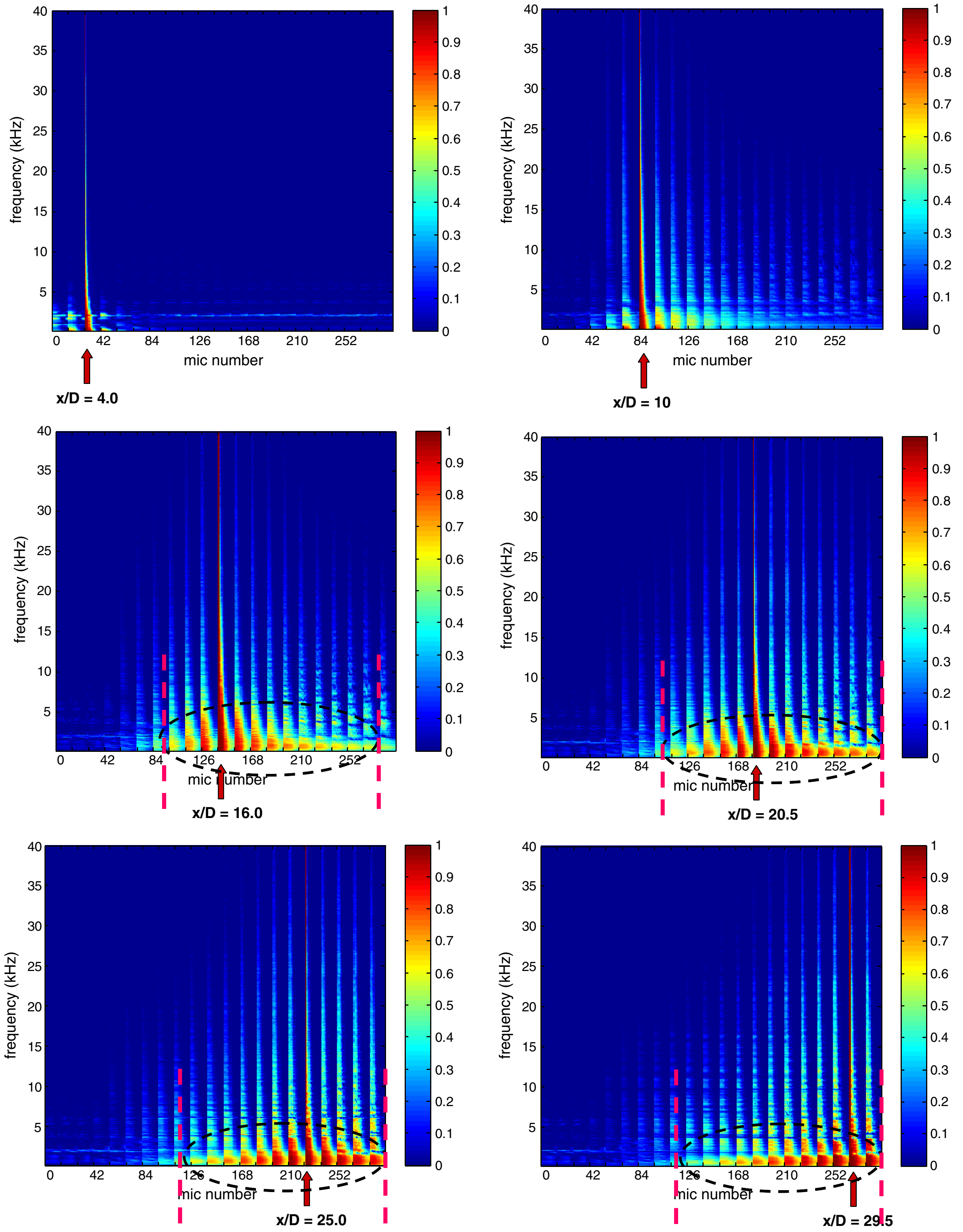

Fig. 14 Variation of the coherence spectra, $M_j = M_d = 1.67$ and $T_t/T_a = 1.0$. Reference microphone at $\phi = 0°$ and $x/D = 4.0$, 10.0, 16.0, 20.5, 25.0, and 29.5.

3) The radial distance at $x/D = 0.0$ is $4.06D$ from the jet centerline, and the cage array spanned a distance of $-5D$ to $25D$.

Thus, near pressure fields were acquired on three different conical surfaces surrounding the jet, from $3D$ to $4.06D$ at the nozzle exit plane. Note that the microphones on the cage array are concentric around the jet axis for these three configurations.

In addition, the entire pressure field was mapped on a plane at an azimuthal angle of 270°, at various radial distances at $x/D = 0.0$ of $2D$, $3D$, $4D$, $5D$, $6D$, $7D$, $8D$, $9D$, $10D$, $12D$, $14D$, $16D$, $18D$, and $20D$. For these measurements of the pressure-field mappings, the axial extent of the array was from the nozzle exit plane $0D$ to $30D$. Pressure signals from all the microphones were recorded for these 14 array positions, even though the locations of the microphones for azimuthal angles other than 270° are not on the plane of interest. For convenience, the array locations described previously are hereafter referred to as positions 1 through 17, in which positions 1–3 are the three axial positions enumerated previously and 4–17 are the radial distances from $2D$ to $20D$, respectively.

There are important differences between the current measurements and those of the UTRC [19–22] and NASA John H. Glenn Research Center at Lewis Field experiments [16]. Whereas the arrays were in the hydrodynamic field in those experiments, the microphones in the current test are located predominantly in the acoustic field and possibly beyond the influence associated with the decaying instability waves on the near-field pressure. A more important difference is the following: the axial extents of the arrays in the studies in [16,19–22,25–30] are $8D$, $10D$ (or $14D$), and $11D$, respectively. As will be shown later with new results, there is a significant shortcoming with these shorter arrays.

III. Results and Discussion

A vast amount of data has been recorded. Simultaneous measurements from all 342 microphones for the 17 array positions resulted in the acquisition and storage of 1.4 terabytes of time-series data. The high-density, simultaneously sampled, space–time data have been processed and analyzed in a variety of ways, including autospectra, cross spectra, coherence spectra, autocorrelation functions, and cross-correlation functions, from which data may be viewed as spectrograms, maps of cross correlations, etc. The coherence function between any two microphones $\gamma_{12}^2(f)$ is defined by

$$\gamma_{12}^2(f) = \frac{|G_{12}(f)|^2}{G_{11}(f)G_{22}(f)}$$

in which G_{11} and G_{22} are the one-sided autospectra, and G_{12} is the cross spectrum between the two signals. Similarly, the cross-correlation coefficient function $\eta_{12}(\tau)$ is defined by

$$\eta_{12}(\tau) = \frac{R_{12}(\tau)}{\sqrt{R_{11}(0)}\sqrt{R_{22}(0)}}$$

in which R_{11} and R_{22} are the autocorrelation functions, R_{12} is the cross-correlation function, and τ represents the time delay. The time-series data are first transformed to the frequency domain, and the coherence functions are calculated. For the calculation of the time-domain correlations, the frequency-domain data are transformed back to the time domain. This procedure allows for the choice of the included frequency range, as this range is shown to have an effect on the correlation functions.

A. Test for Acoustic Interference of Cage Array

First, the acoustic interference of the cage array is established. An examination of Fig. 3 indicates that there is a dense layout of microphones and a substantial supporting structure surrounding the jet at azimuthal angles spanning 180–360 deg. The extent of reflections of acoustic signals from the array on the measured far-field spectra was assessed to establish the array's interference effect. First, far-field spectral measurements were made at several jet operating conditions before the installation of the cage array; then, the measurements were repeated with the array located closest to the jet (position 1), at the largest radial distance away (position 17) and with the array stowed. Sample results from the different far-field arrays are presented. Figure 5 shows spectral comparisons from three unheated jets with Mach numbers of 0.5, 0.6, and 0.9 at several polar angles of 90, 120, and 140° and at an azimuthal angle of 90°. These comparisons and others (not included) show that the spectra at $\phi = 90°$ are not subject to any noticeable reflections from the cage array. Figure 6 shows spectral comparisons for the microphone arrays at azimuthal angles of 60 and 30° for a heated jet with $M_j = 0.9$ and $T_t/T_a = 3.2$. There is excellent agreement, indicating the lack of any substantive reflections from the cage array for these microphone arrays as well. Figures 7 and 8 show comparisons for the microphone array at $\phi = 5°$. There are interesting differences: for subsonic unheated jets, the effect of reflections (say at 140°) is minor and confined to the high-frequency regime. For the supersonic unheated jet in Fig. 8, however, the effect of the cage array is very pronounced, with a substantial drop in the spectral levels. There is a simple explanation for this trend; an examination of the bottom portion of the array in Fig. 3 indicates that the metal rings extend beyond $\phi = 0°$. The extra length was needed for holding each ring during the machining and manufacturing process. Unfortunately, the length was such that it blocked the line of sight to the microphones located at $\phi = 5°$. Because of time constraints, the microphones could not be moved to say $\phi = 10°$ to avoid this problem. The low-frequency portions of the spectra in Fig. 8 are unaffected; the acoustic rays with long wavelengths are not impacted. However, the high-frequency levels are lower due to scattering from the ring extensions. Thus, the high-frequency levels are impacted for the far-field microphones at $\phi = 5°$ with the cage array in positions 1–3. The main conclusion from this section is the following: the presence of the cage array with a dense layout of microphones, even when positioned close to the jet, does not cause any significant reflections for the spectra measured at the three far-field microphone arrays at $\phi = 90$, 60, and 30°.

B. Effect of Frequency Range on Correlation Functions

An interesting problem came to light when the space–time correlations were calculated. This problem is highlighted with the following analysis. Figure 9 shows the variation of the coherence function for the following jet conditions: $M_j = M_d = 1.67$ and $T_t/T_a = 1.0$. The reference microphone is at $x/D = 10.0$ and $\phi = 0°$. The second microphone is located at $x/D = 10.0$, and ϕ varies from 5 to 45°. The correlation levels are high for the very low frequencies, ~0.8 for an azimuthal separation of 45°. The levels drop with increasing frequency, particularly rapidly with increasing azimuthal separation. Further, the coherence levels are close to the electronic noise floor for all frequencies ≥ ~40 kHz. The length of the potential core for this jet is ~$8D$, based on the equations established in [47,48]. Figure 10 shows the axial variations of the coherence functions for the same jet; the reference microphone is at $\phi = 0°$ and $x/D = 10.0$. The second microphone is located at $\phi = 0°$, and x/D varies from 7.0 to 16.0. Note that the frequency range on the x-axis is restricted to an upper limit of 40 kHz in this figure. Again, the lower-frequency signals have higher correlations.

Analyses of a larger set of data indicate that there is little coherence for frequencies above ~40 kHz. The axial spacing of the microphones is $1.5D$ ($D = 2.45$ in.), as already noted. This distance

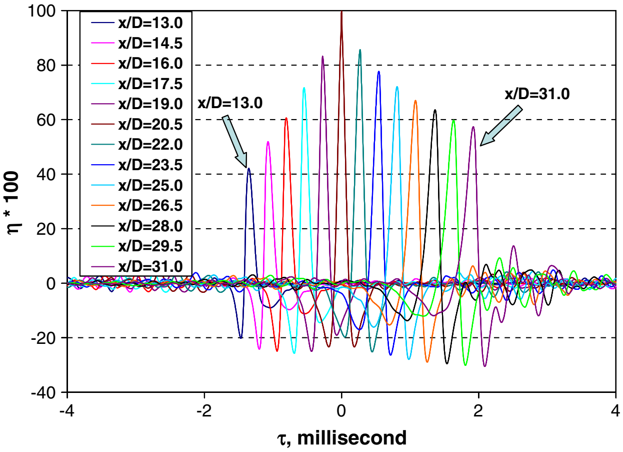

Fig. 15 Axial correlation, $M_j = M_d = 1.67$ and $T_t/T_a = 1.0$. Reference microphone at $\phi = 0°$ and $x/D = 20.5$. Second microphone at $\phi = 0°$ and $x/D = 13.0$ to 31.0.

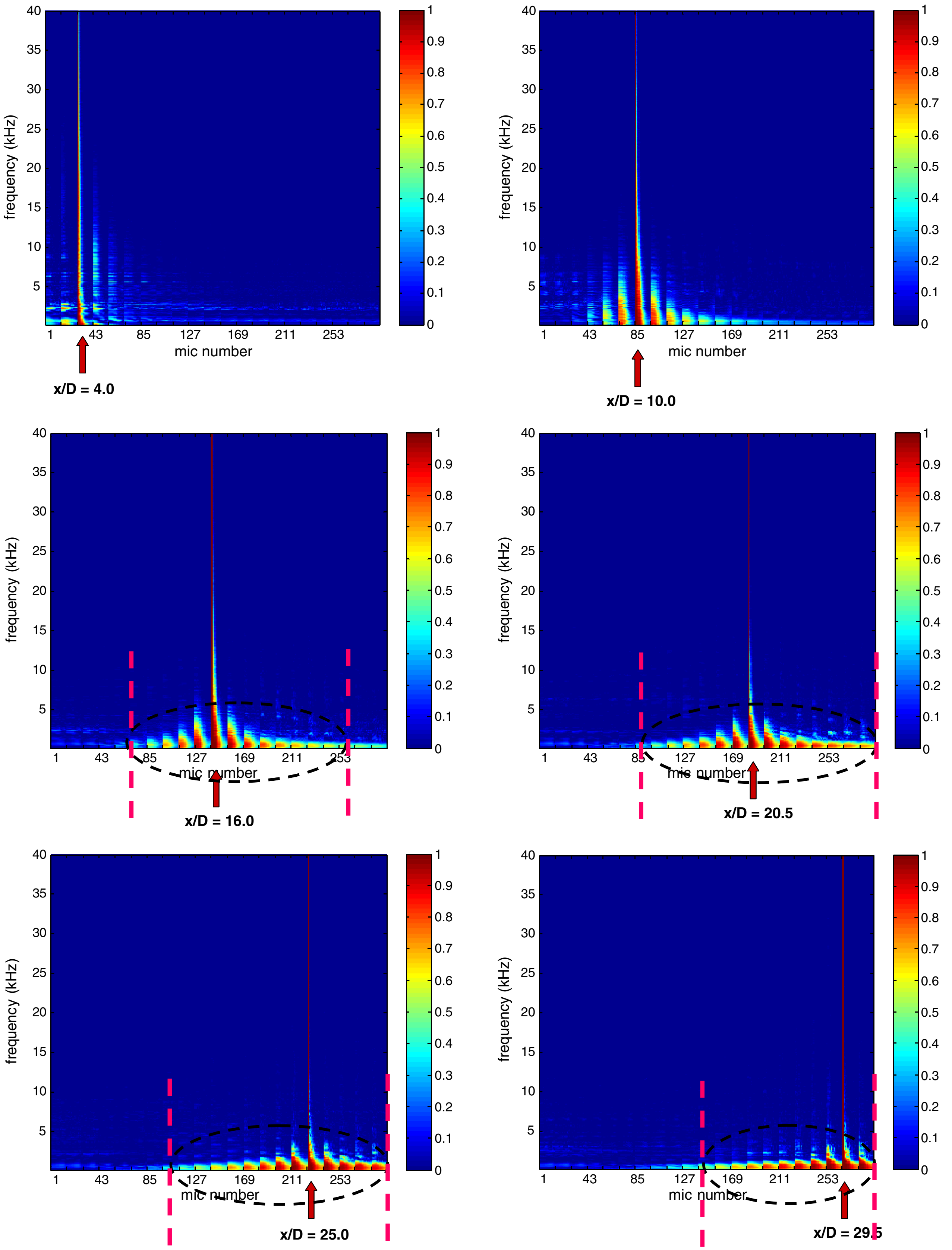

Fig. 16 Variation of the coherence spectra, $M_j = M_d = 1.67$ and $T_t/T_a = 3.2$. Reference microphone at $\phi = 0°$ and $x/D = 4.0, 10.0, 16.0, 20.5, 25.0,$ and 29.5.

corresponds to a wavelength of 0.31 ft, with an associated frequency of 3670 Hz. However, measurable coherence is observed up to a frequency of ~40 kHz, which is roughly 10 times the frequency associated with the array resolution. Because of this, it is thought that the lack of coherence at still higher frequencies is not related to the array resolution.

For the time-domain analyses, though, there is a pronounced impact of the included frequency range on the width and the shape of

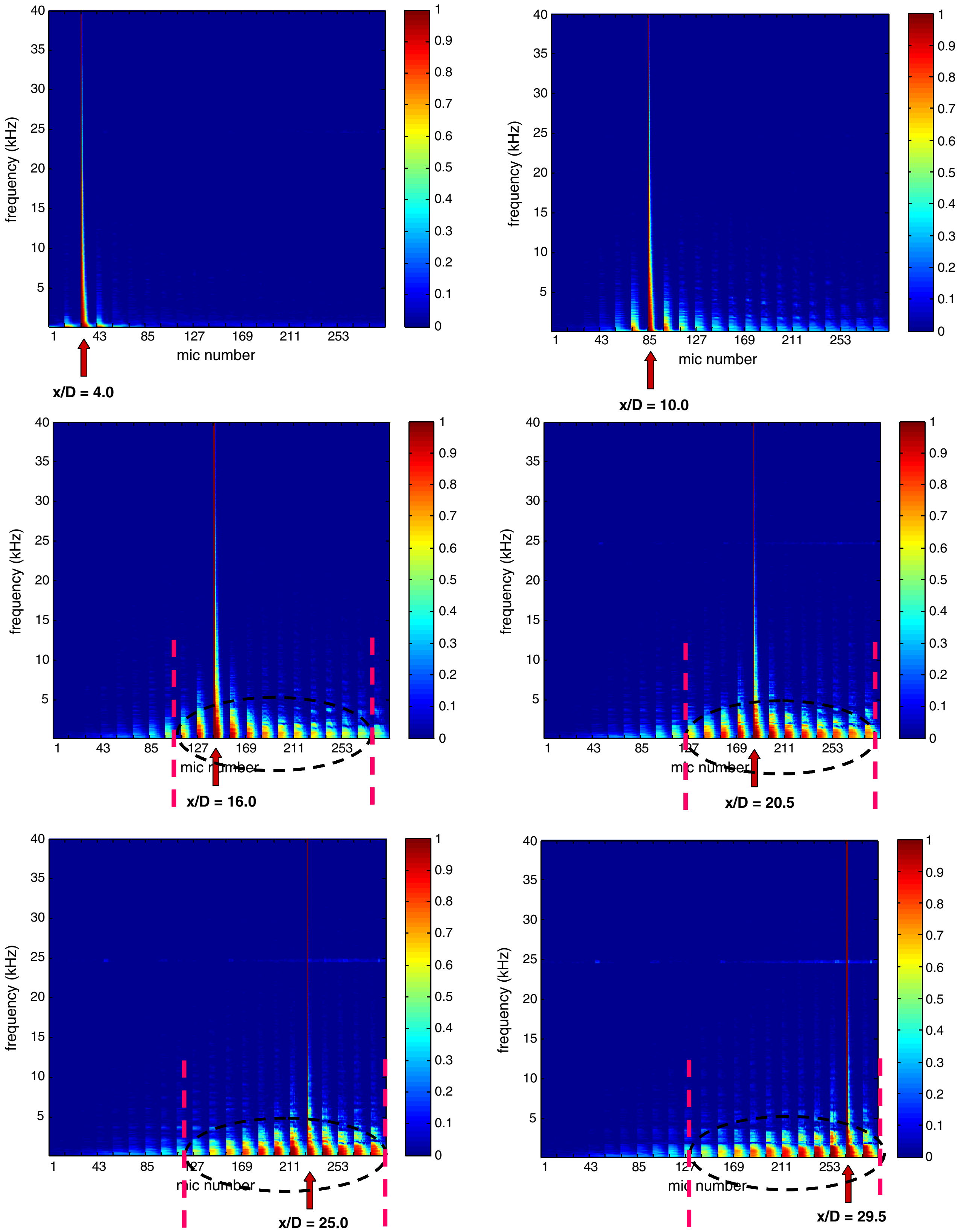

Fig. 17 Variation of the coherence spectra, $M_j = 0.51$ and $T_t/T_a = 1.0$. Reference microphone at $\phi = 0°$ and $x/D = 4.0, 10.0, 16.0, 20.5, 25.0$, and 29.5.

the correlation function. Figure 11 shows the autocorrelation functions at two different microphone locations of $x/D = 7.0$ and 13.0, both at $\phi = 0°$. In the calculations of the time-domain correlations, the low-pass filters are set at desired limits, and the correlation functions are generated. There are two consequences with the inclusion of the uncorrelated high-frequency "noise" in the analysis:

1) The width of the correlation function becomes narrower.

2) Several wiggles are introduced near the foot of the correlation function.

Figure 12 shows a similar effect on the azimuthal cross-correlation functions; again, $M_j = M_d = 1.67$ and $T_t/T_a = 1.0$, and the reference microphone is $x/D = 13.0$ and at $\phi = 0°$. The peak correlation levels drop progressively with the inclusion of the

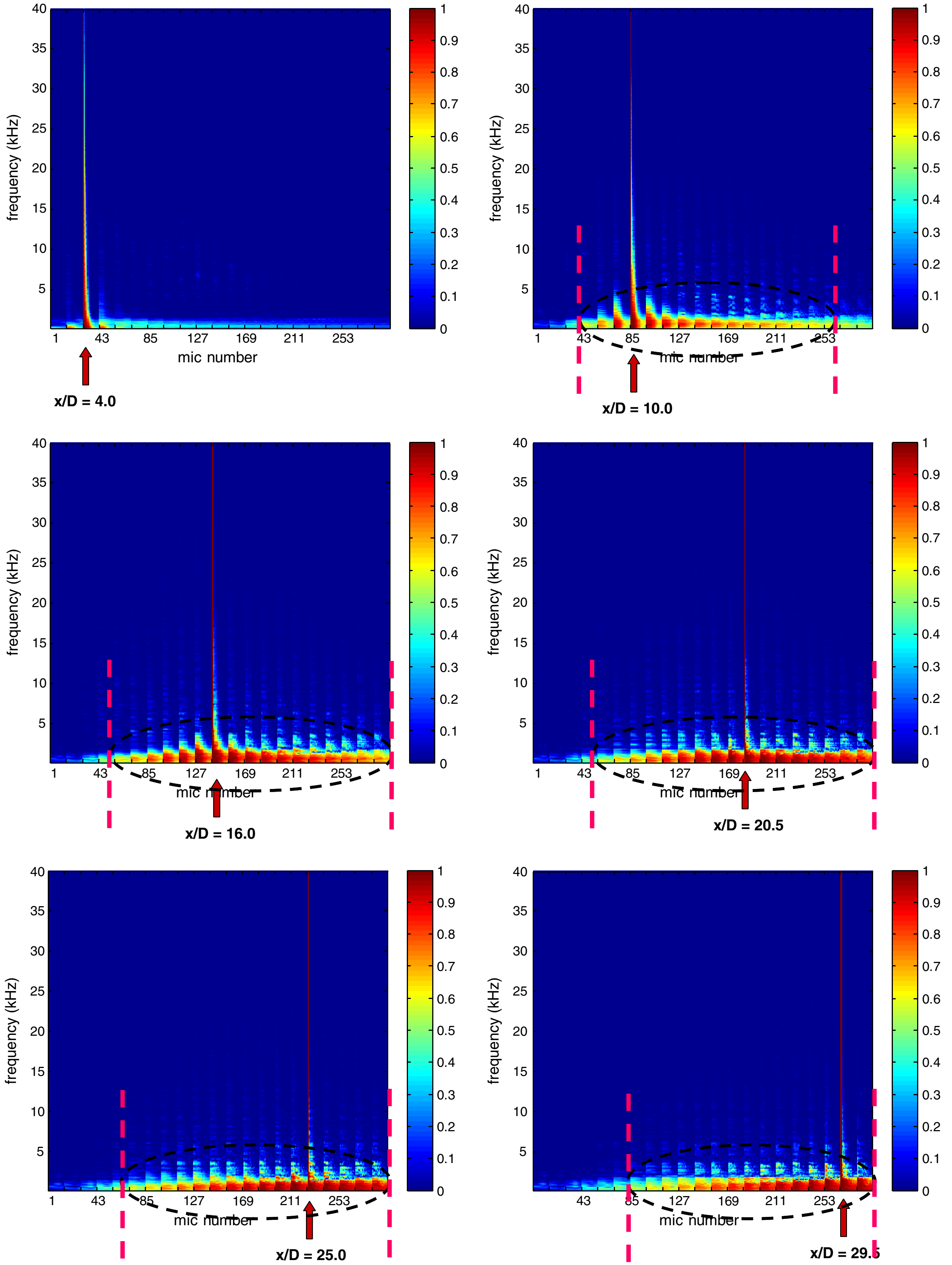

Fig. 18 Variation of the coherence spectra, $M_j = 0.5$ and $T_t/T_a = 3.2$. Reference microphone at $\phi = 0°$ and $x/D = 4.0, 10.0, 16.0, 20.5, 25.0$, and 29.5.

less-correlated high-frequency signals in the computation of the correlation functions. For example, there is a reduction of ~0.2 (20%) for a separation angle of 15° when the included frequency range is increased from 200 Hz–10 kHz to 200 Hz–80 kHz. The effect of the bandwidth is thus seen to have a strong effect on the computed correlation functions. The effects of jet Mach number and velocity V_j/a also have a strong bearing on the source strength and frequency content. In the generation of the correlation functions, the entire frequency range of 200 Hz to 80 kHz is used; this step maintains consistency for all the test points.

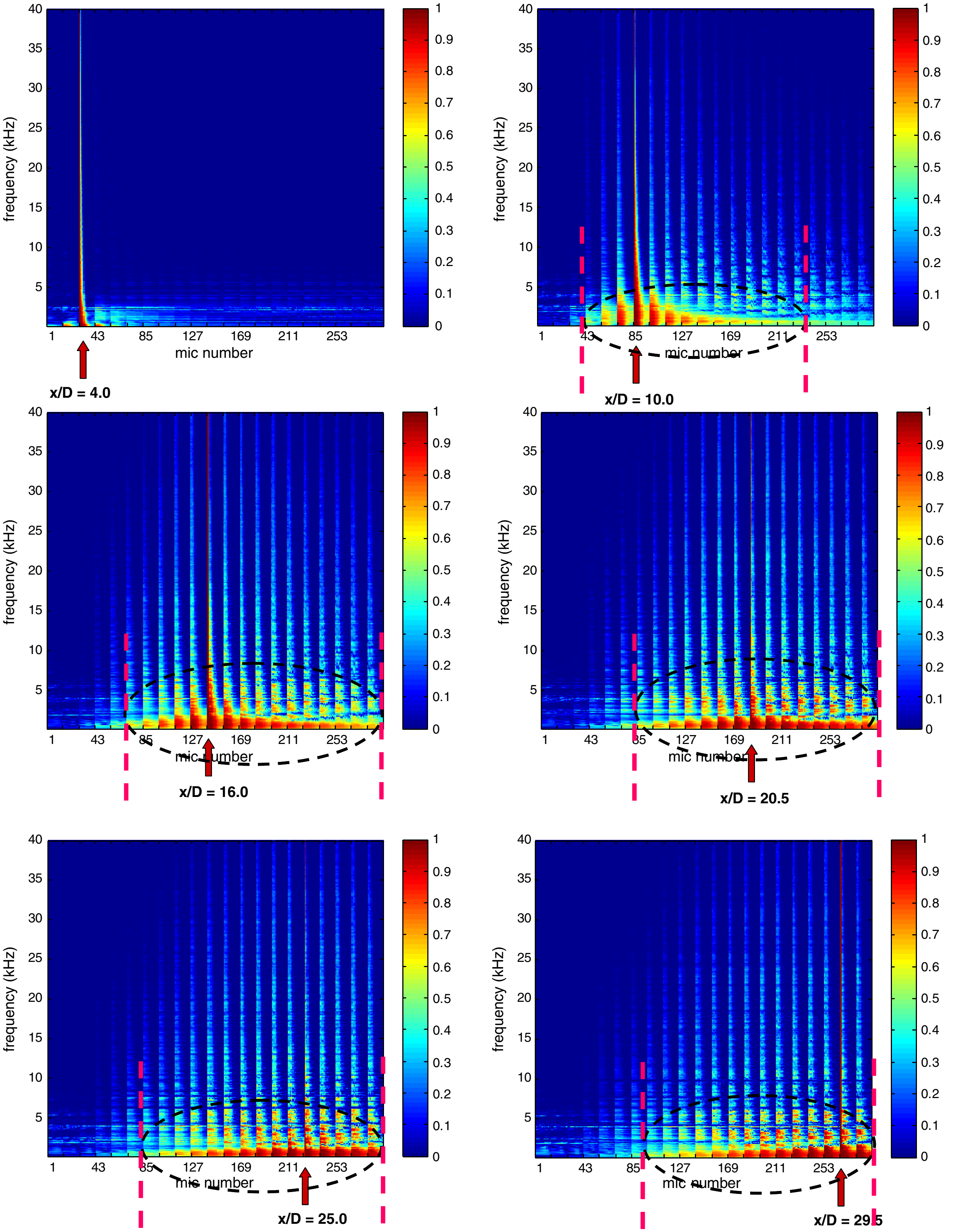

Fig. 19 **Variation of the coherence spectra, $M_j = 0.9$ and $T_t/T_a = 3.2$. Reference microphone at $\phi = 0°$ and $x/D = 4.0$, 10.0, 16.0, 20.5, 25.0, and 29.5.**

C. Near-Field Space–Time Characteristics

The variations of the near-field space–time characteristics for different jet conditions are now presented. Figure 13 depicts the azimuthal variations of the coherence function for the jet with $M_j = M_d = 1.67$ and $T_t/T_a = 1.0$. The convective Mach number is 0.93. The reference microphone is at $x/D = 4.0$ and $\phi = 0°$ and $x/D = 16.0$ and $\phi = 0°$, respectively. Recall that a similar plot for the reference microphone at $x/D = 10.0$ and $\phi = 0°$ is already presented in Fig. 9. At all locations, the values of the correlations decrease with increasing frequency. This trend becomes more pronounced as the separation angle from the reference microphone increases. However, there are also distinct differences when the reference microphone is moved from $x/D = 4.0$ to 10.0 and 16.0: there is a steep decrease in correlation levels with separation angle when the microphone is at $x/D = 4.0$, whereas the signals are more correlated at the larger downstream distances.

A global variation of the coherence levels is obtained with contour maps, as shown in Fig. 14 for $M_j = M_d = 1.67$ and $T_t/T_a = 1.0$. The location of the reference microphone at $\phi = 0°$ is progressively moved downstream, and the correlations with all the microphones in the array are presented. Selected coherence spectra with the reference microphone at six x/D locations of 4.0, 10.0, 16.0, 20.5, 25.0, and 29.5 are displayed in these types of plots at different jet operating conditions. The arrows indicate the location of the reference microphone is these figures. The parameter on the x-axis is the microphone number; each tick mark on the x-axis corresponds to 14 microphones: that is, one ring in the cage, at a fixed x/D. In this notation, each division also denotes an axial distance of $1.5D$. The frequency range on the y-axis is restricted to a maximum value of 40 kHz.

There is very little coherence when the reference microphone is located at $x/D = 4.0$. For $x/D = 10$, a definitive trend starts to emerge, with good correlations over a few diameters. When the reference microphone is at $x/D \geq 16$, dramatic changes in the contour maps are observed. Color contours from green/yellow to red represent coherence levels of ≥ 0.5 (or 50%). The axial extent of regions of high coherence, arbitrarily taken to be ≥ 0.5, is highlighted by dashed ovals and vertical dashed lines. There is a very large source that is coherent over an axial extent of $\sim 15D$ and nearly all around the periphery of the jet (360°). The high-coherence levels are generally confined to the lower frequencies. An examination of the data in the time domain reinforces this trend; Fig. 15 shows the correlation functions, with the reference microphone at $\phi = 0°$ and $x/D = 20.5$ and the second microphone at $\phi = 0°$ and x/D over a range of 13.0 to 31.0. The maximum correlation level is ≥ 0.4 (or 40%) for the entire range of axial distance, with significantly higher correlations of $\geq \sim 0.6$ from $x/D = 16.0$ to 29.0. Figure 16 shows a coherence contour map for a heated jet with $M_j = M_d = 1.67$ and $T_t/T_a = 3.2$. The convective Mach number is 1.69. The characteristics are similar to those observed for the unheated supersonic jet in Fig. 14. However, the range of frequencies for which there is high correlation is much smaller. Again, there is a large coherent source with an axial extent of $\sim 15D$.

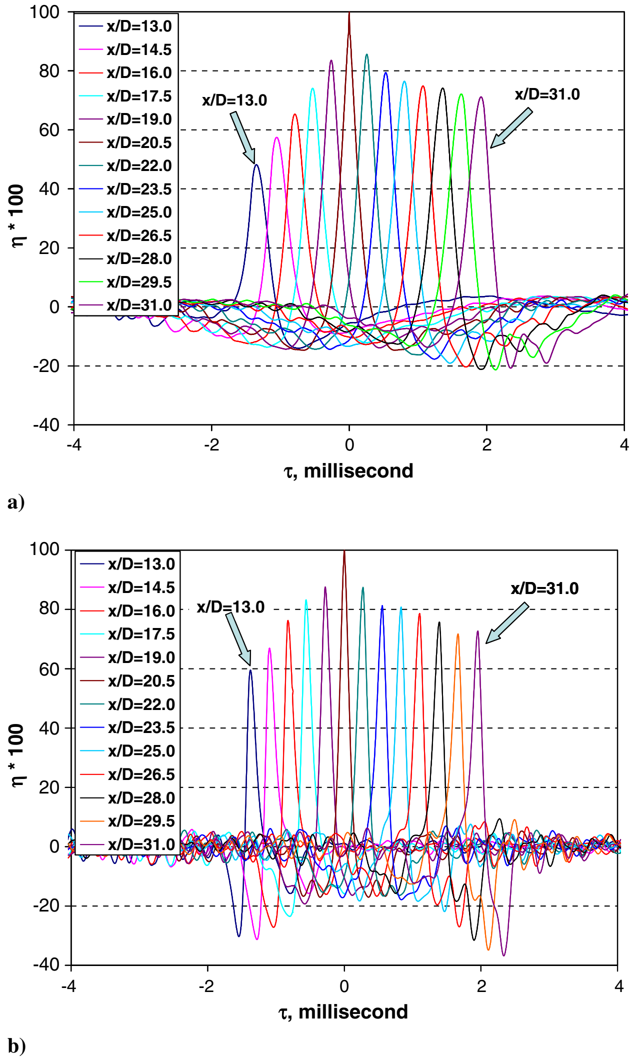

Fig. 20 Axial correlation, reference microphone at $\phi = 0°$ and $x/D = 20.5$; $r/D = 3.0$ at $x/D = 0.0$. Second microphone at $\phi = 0°$ and $x/D = 13.0$ to 31.0: a) $M_j = 0.51$ and $T_t/T_a = 1.0$ and b) $M_j = 0.9$ and $T_t/T_a = 3.2$.

Next we turn our attention to subsonic jets. Three test conditions with 1) $M_j = 0.51$ and $T_t/T_a = 1.0$, 2) $M_j = 0.51$ and $T_t/T_a = 3.2$, and 3) $M_j = 0.9$ and $T_t/T_a = 3.2$ are considered. The corresponding convective Mach numbers are 0.36, 0.64, and 1.05, respectively. First, the coherence contour maps for these three cases are presented in Figs. 17–19. First of all, there are striking resemblances in terms of low correlations for reference microphones closer to the nozzle exit ($x/D = 4.0$) and progressively increasing correlations farther downstream. There is a large coherent source starting at $\sim 12D$ from the nozzle exit plane and extending for $\sim 15D$. There are also notable differences: for the unheated jet, the correlated region is fairly limited in extent when the reference microphone is at $x/D = 10.0$, whereas there is extended correlation for the heated subsonic jets. Further, higher levels of coherence are observed over a larger frequency range for the $M_j = 0.9$ and $T_t/T_a = 3.2$ jet. When all five contour maps are examined, an interesting trend becomes evident: wider range of frequencies with high levels of correlations is observed only for the $M_j = 0.9$ and $T_t/T_a = 3.2$ and $M_j = M_d = 1.67$ and $T_t/T_a = 1.0$ jets. The reasons are not entirely clear as of now.

To get a perspective on the coherent source, correlation functions in the time domain for the $M_j = 0.51$, $T_t/T_a = 1.0$, and $M_j = 0.9$ and $T_t/T_a = 3.2$ jets are investigated. As in the supersonic jet, the reference microphone is at $\phi = 0°$ and $x/D = 20.5$ and the second microphone at $\phi = 0°$ and x/D over a range of 13.0 to 31.0. Figures 20a and 20b depict the correlation functions for these two cases, respectively. As in the supersonic jet, the maximum correlation level is ≥ 0.4 (or 40%) for this entire axial distance of $18D$ for the low-speed jet. Curiously, the maximum correlation is ~ 0.7 for the axial distance of $21D$ to $31D$ for both subsonic jets; note that the maximum correlation values are higher than those for the supersonic jet. One big difference between the correlation functions for the low-speed and high-speed jets is the following: there are no strong negative loops for the low-speed jet. In addition, the width of the main loop is wider for the low-speed jet. Apart from these features, a strong coherent source that extends for $\sim 18D$ is observed for jets at all velocities (results for other cases are not included in this paper) regardless of the convective Mach number, which spans a range of 0.36 to 1.69.

A pertinent question that must be considered is the following: what happens to the correlations when the microphones are moved closer to the jet? Recall that $r/D = 3.0$ at $x/D = 0.0$ for the correlations shown in Figs. 14–20. To answer this question, the correlation functions with the microphones at $r/D = 2.0$ at $x/D = 0.0$ are examined. Comparable plots for the three jet conditions, the unheated $M_j = 1.67$ and 0.51 jets and the heated $M_j = 0.9$ and $T_t/T_a = 3.2$ jet, are shown in Fig. 21. Note that the location of the reference microphone is different: $x/D = 19.5$ and $\phi = 90°$. First of all, there are striking similarities between the trends seen in this plot and those in Figs. 15 and 20. The maximum correlation levels are slightly lower when the microphones are moved closer to the jet axis; this reduction seems to suggest that the effects of the hydrodynamic field possibly prevail at the closer r/D. However, the main conclusion that there is a large coherent source, $\sim 18D$ in axial extent, still stands. Thus, consistent trends are observed for both the array locations.

For the sake of completeness, a similar plot of the axial correlation is shown in Fig. 22. The jet operating conditions are $M_j = 1.67$ and $T_t/T_a = 1.0$. The reference microphone is now at $\phi = 0^\circ$ and $x/D = 20.5$, and $r/D = 4.06$ at $x/D = 0.0$. The second microphone is at $\phi = 0^\circ$, and x/D covers a range of 13.0 to 25.0. Recall that the whole cage array is moved upstream by $6D$ to move the microphones radially outward to $4.06D$; this move brings the last ring to $x/D = 25.0$. Comparable correlations at two other radial distances of $3D$ and $2D$ have already been presented in Figs. 15 and 21a. A comparison of all three plots indicates that the overall trends are identical at all three radial locations. Furthermore, the peak correlation levels at $r/D = 3.0$ and $r/D = 4.06$ for the microphones in the downstream direction are almost the same; there is a slight reduction in peak correlation levels in the upstream direction. These three figures provide a feel for the location of the microphones in the near-hydrodynamic and propagation regions of the jet.

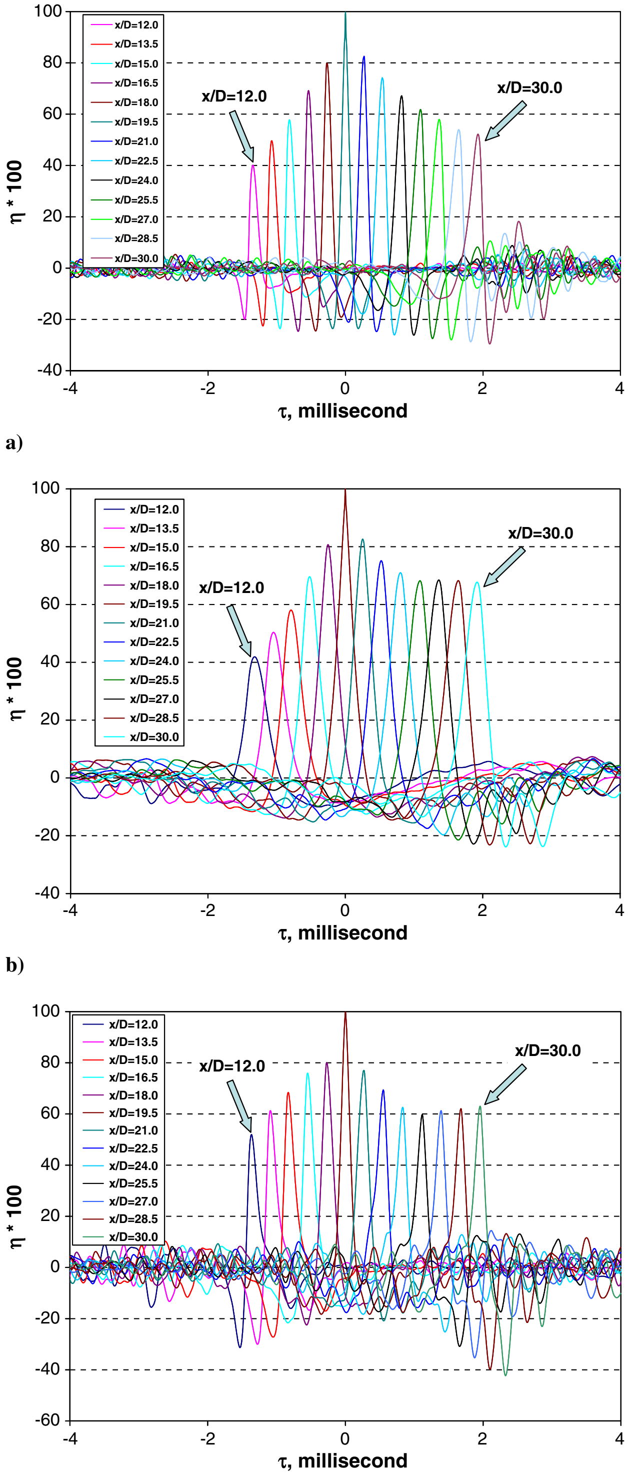

a)

b)

c)

Fig. 21 Axial correlation, reference microphone at $\phi = 90^\circ$ and $x/D = 19.5$; $r/D = 2.0$ at $x/D = 0.0$. Second microphone at $\phi = 90^\circ$ and $x/D = 12.0$ to 30.0: a) $M_j = 1.67$ and $T_t/T_a = 1.0$, b) $M_j = 0.51$ and $T_t/T_a = 1.0$, and c) $M_j = 0.9$ and $T_t/T_a = 3.2$.

It should be kept in mind that the time-domain correlations have been normalized by the autocorrelations with zero time delay. It is instructive to examine the axial variations of the maximum autocorrelation levels at different jet conditions. Such a variation is shown in Fig. 23 for six jet conditions: $M_j = 0.51$, 0.9, and 1.67, at two temperature ratios of $T_t/T_a = 1.0$ and 3.2. There is the expected increase in level with increasing jet velocity, as the higher-velocity jet radiates higher levels of noise to the far field. The maximum levels are comparable for the unheated supersonic jet ($M_c = 0.93$) and the heated subsonic jet ($M_c = 1.05$), because the convective Mach numbers are not dissimilar. The trends over the entire axial distance are similar for the two subsonic jets with comparable convective Mach numbers of 0.58 ($M_j = 0.9$ and $T_t/T_a = 1.0$) and 0.64 ($M_j = 0.51$ and $T_t/T_a = 3.2$). The peak locations for maximum pressure occur at $\sim 6D$–$\sim 8D$ for all the jets; thus, the peak locations are observed near the end of the potential cores for all the jets. However, the peak coherent source is located from $\sim 13D$ to $\sim 31D$, as seen in Figs. 14–21 and highlighted by the shaded oval in Fig. 23. That is, the strong coherent source is located well beyond two potential core lengths from the nozzle exit. This is an important new finding and is contrary to existing belief. It is also worth pointing out, that this large coherent source was completely missed in the prior investigations with near-field arrays because of the shorter axial extents of the arrays.

An overall analysis of the results reported in this section, in Figs. 13–23, together with the source distributions shown in Figs. 1 and 2 would be appropriate at this juncture. The current measurements have revealed an extended region of highly coherent pressure fluctuations in the near field, and this region lies well downstream of the end of the potential core of the jet. As per existing belief based on old data, the peak noise source is located near the end of the potential core; the measurements in the near field could then represent the propagated noise field from this source. This is a plausible interpretation, based on old data. The source distribution measured with the elliptic mirror indicates a large source region, especially for the low frequencies from $\sim 10D$ to $\sim 30D$. The large coherent region, from $\sim 13D$ to $\sim 31D$, observed in the near-field contour plots in Figs. 14 and 16–19, is concentrated at the very low frequencies, typically $\leq \sim 3000$ Hz. That is, there is a precise overlap of these two regions. Recall the premise that the features of the true acoustic sources would be imprinted on the near-field pressure correlations. The consistent and mutually supporting observations from the two

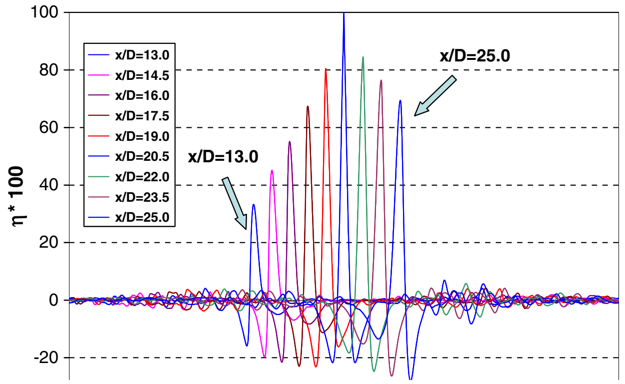

Fig. 22 Axial correlation, reference microphone at $\phi = 0^\circ$ and $x/D = 20.5$; $r/D = 4.06$ at $x/D = 0.0$. Second microphone at $\phi = 0^\circ$ and $x/D = 13.0$ to 25.0. $M_j = 1.67$ and $T_t/T_a = 1.0$.

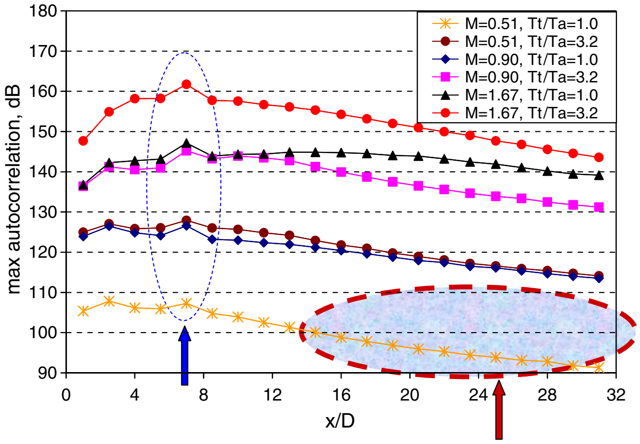

Fig. 23 Axial variation of maximum autocorrelation at each x/D. $M_j = 0.51, 0.9$, and 1.67; $T_t/T_a = 1.0$ and 3.2. Peak locations highlighted by arrow at $x/D \sim 6$. Location of large coherent source, from x/D of $\sim$13 to 31, highlighted by shaded oval.

different sets of measurements reinforce this supposition. Therefore, there is reason to believe that the large region of highly coherent pressure fluctuations represents an equivalent source.

D. Near-Field–Far-Field Correlations

The correlations between near-field and far-field signals are presented in this section. Recall that there are three far-field arrays: one polar arc at fixed distance and two at fixed sideline distances. For the correlations with the polar array, the time delay for the propagation of sound to the far field is nearly constant; because of this, the peaks in the correlation functions from a fixed near-field position to the different polar angles lie on top of each other. This is not the case for the array at a fixed sideline distance, as the distance to the microphone and consequently the time of propagation to each microphone vary with radiation angle. Therefore, correlations with the microphones at the fixed sideline distance at an azimuthal angle of 60° are shown. Sample correlation functions for the $M_j = 0.9$ and $T_t/T_a = 3.2$ jet, with the reference microphones at $\phi = 0°$ and $x/D = 7.0$, 10.0, 13.0, and 16.0 with far-field microphones in the polar angular range of 120 to 150°, are displayed in Fig. 24. As expected, the peaks occur at increasing time delays with increasing radiation angle. There is also in interesting variation in the maximum peak levels with different locations for the reference microphone. The maximum level has the lowest values for an angle of 120°; there is no discernible correlation above the electronic noise floor for an angle of 110°, which is included in the plot with the reference microphone at $x/D = 10.0$. The maximum levels begin to increase, as we move aft to larger inlet angles, and reach values of ≥ 0.65 (65%). The peak contributions to the different angles from different locations of the jet also change. Similar trends are observed at other reference locations farther downstream and at other jet operating conditions.

An overall picture of the noise radiation from different portions of the jet to particular radiation angles is obtained when the axial variations of the maximum correlation levels with angle are examined. The effect of heating the jet from $T_t/T_a = 1.0$ to 3.2 at three different Mach numbers of 1.67, 0.9, and 0.51 are investigated in this fashion. The supersonic jet is first considered in Fig. 25. There is close to zero correlation with all the angles when the near-field

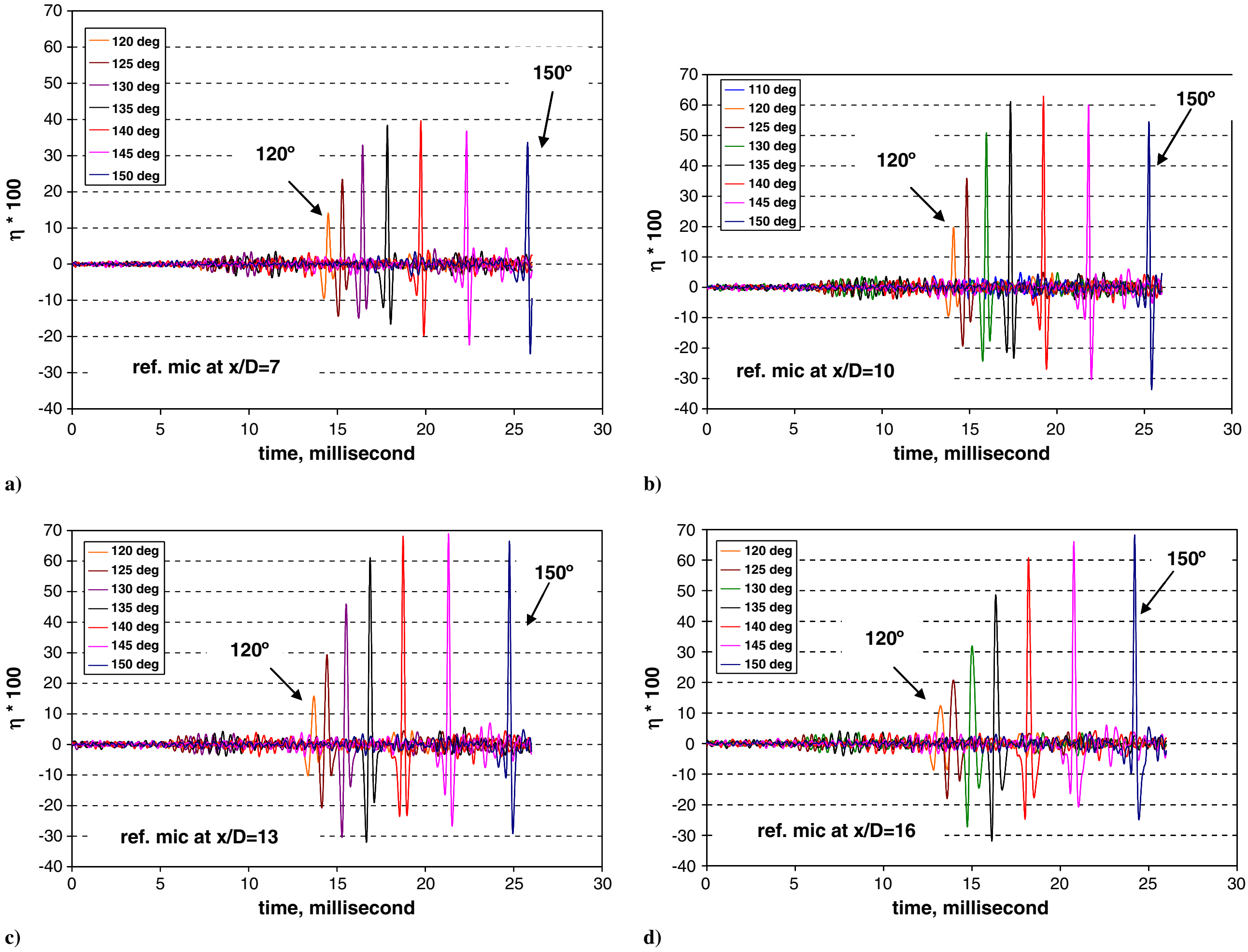

Fig. 24 Near-field–far-field correlation, $M_j = 0.9$ and $T_t/T_a = 3.2$. Reference microphone at various x/D and $\phi = 0°$.

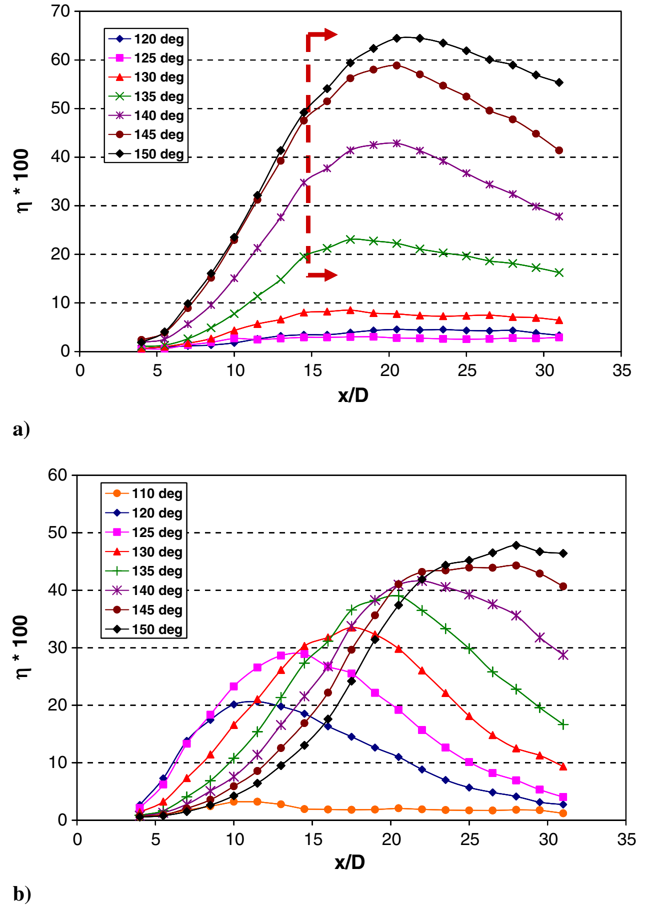

Fig. 25 Peak near-field–far-field correlations. Reference microphone at all x/D and $\phi = 0°$. Far-field microphones at 120 to 150°: a) $M_j = 1.67$ and $T_t/T_a = 1.0$ and b) $M_j = 1.67$ and $T_t/T_a = 3.2$.

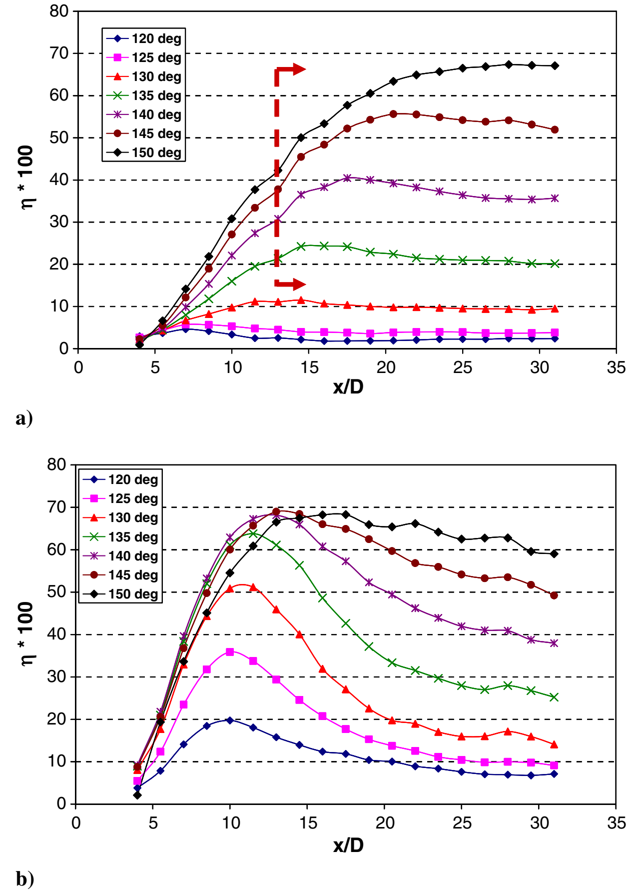

Fig. 26 Peak near-field–far-field correlations. Reference microphone at all x/D and $\phi = 0°$. Far-field microphones at 120 to 150°: a) $M_j = 0.9$ and $T_t/T_a = 1.0$ and b) $M_j = 0.9$ and $T_t/T_a = 3.2$.

point is located at $x/D \leq \sim 7$ for the unheated jet. Further, the correlation levels are <0.1 (10%) for radiation angles <130°, for all the near-field locations. The peak levels start to increase dramatically with x/D as the radiation angle is increased: a maximum level of ∼0.65 is reached for the microphone at 150°. The observed trends for the heated supersonic jet are markedly different:

1) There is a measurable level of correlation for the lower radiation angles of 120 to 130°, with the maximum level of ∼0.33 for 130°.

2) The peaks for the lower angles occur at distances that are closer to the nozzle exit.

3) There is a well-defined progression of peak axial distance from the nozzle exit plane with increasing radiation angle from 120 to 140°.

4) There is virtually no correlation for 110°, even for this highly heated jet.

5) There is also a rapid decay in the correlation levels with downstream distance beyond the peak location.

The high-subsonic jet with $M_j = 0.9$ is considered next, in Fig. 26. As in the unheated supersonic jet, the correlation levels are low and of the order of $< \sim 0.1$ (10%) for radiation angles <130°. High peak correlations are observed at large aft angles, with a value of ∼0.65 at 150°. The characteristics for the heated jets are again different from those for the unheated jet: measurable correlation levels are observed for 120 to 130°, and the distance of the peak axial location from the nozzle exit increases with increasing radiation angle. Though there are similarities between the trends for the $M_j = 0.9$ and 1.67 jets at $T_t/T_a = 3.2$, there is also a big difference: for the $M_j = 1.67$ jet, there is a slower initial growth for the peak values and a longer initial region of low correlations, which increases monotonically with increasing radiation angle; for the $M_j = 0.9$ jet, the peak values start rising immediately from $x/D = \sim 5$, and the peak correlation levels are reached by $x/D = 13$ for all the angles.

Finally, the low-subsonic jet with $M_j = 0.51$ is investigated in Fig. 27. Similar to the characteristics for the higher-Mach numbers, the trends are different for the heated and unheated jets. The pattern of noticeable correlation in the angular range of 120 to 130° is once again observed for the heated jet. Furthermore, there is a gradual decay of the correlation following a rapid growth at these lower angles for the heated jet. Peak correlation levels of ∼0.8 (80%) are observed over an extended axial distance, from $x/D = 13$ to $x/D = 31$, for large aft angles ≥ 145°. The peak correlation levels for all the jets at an angle of 150° ranges from ∼0.48 to ∼0.83. The lowest peak correlation level occurs for the heated $M_j = 1.67$ and the highest level for the heated $M_j = 0.51$ jet. It is important not to interpret these raw numbers as implying that the lower-Mach-number jet has higher source strength, for the following reason: these are normalized correlation levels. The autocorrelation levels change with x/D and jet conditions, as shown in Fig. 23. The fundamental conclusions from these plots are as follows:

1) There is a large coherent source region that predominantly radiates to the aft angles for jets at all convection Mach numbers, from 0.36 to 1.69.

2) This source is located from $\sim 13D$–$\sim 31D$, which is well beyond the end of the potential core.

In this regard, the noise radiation mechanism responsible for large aft angles seems to be the same regardless of jet velocity. This point will be further reinforced in the following sections.

The reason for the noticeable correlation in the angular range of 120 to 130° for the heated jets is now investigated with an examination of the spectral shapes in the far field. Figure 28 shows the variation of the spectral shape for a jet with $M_j = 1.0$ and $T_t/T_a = 3.2$. The band number on the x-axis is defined as $10 \times \mathrm{Log}_{10}(f)$, in which f is frequency in Hertz. The spectra in the angular range of 90 to 150°, and comparisons with the similarity spectra are shown. At

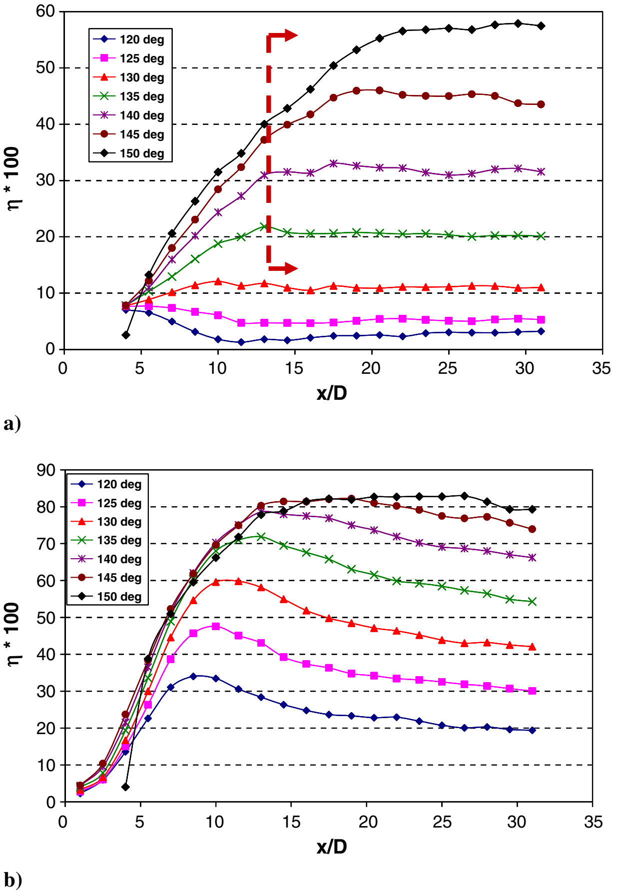

Fig. 27 Peak near-field–far-field correlations. Reference microphone at all x/D and $\phi = 0°$. Far-field microphones at 120 to 150°: a) $M_j = 0.51$ and $T_t/T_a = 1.0$ and b) $M_j = 0.51$ and $T_t/T_a = 3.2$.

the lower polar angles of 90 and 110°, the spectral peaks are broad and conform to the shapes of the fine-scale similarity spectrum. At an angle of 120°, the spectral shape changes, and there is some contribution from the large-scale structures; at this angle, there is contribution from both sources, as highlighted by the arrow and the slanted lines. As the radiation angle increases, the contributions from the large-scale turbulence become progressively more dominant, and the spectrum finally conforms to that of the large similarity spectrum at 150°. Note that the spectral peak is narrow. Viswanathan [45] showed from far-field correlation measurements that there is virtually no correlation when the spectral shape conforms to the fine-scale similarity shape, and there is significant correlation when the spectral shape conforms to the large-scale similarity shape. For the unheated jet, the spectra up to 130° are characterized by the fine-scale similarity shape. Perhaps it should not be surprising, then, that there are noticeable near-field–far-field correlations, because of the contributions from the coherent structures in the angular range of 120 to 130° for these highly heated jets with $T_t/T_a = 3.2$.

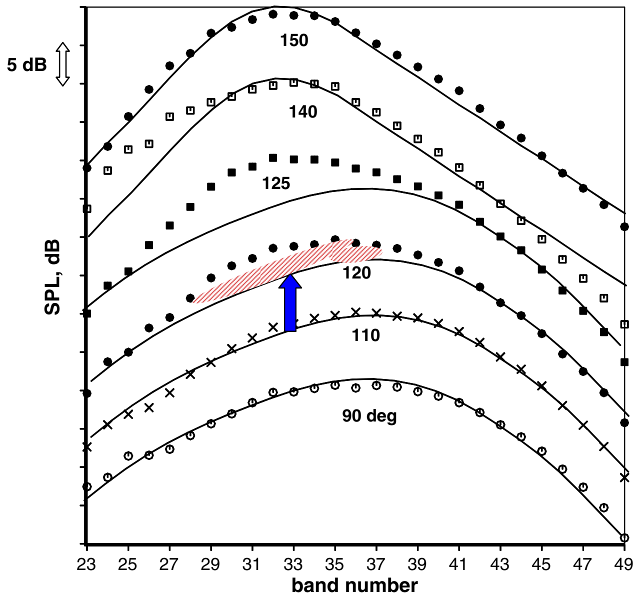

Fig. 28 Variation of the spectral shapes with angle and comparisons with the similarity spectra, $M_j = 1.0$ and $T_t/T_a = 3.2$.

E. Near-Field Mapping of Pressure Field

Sample contours of both the OASPL and specific frequencies are investigated to elucidate the nature of the noise radiation and the

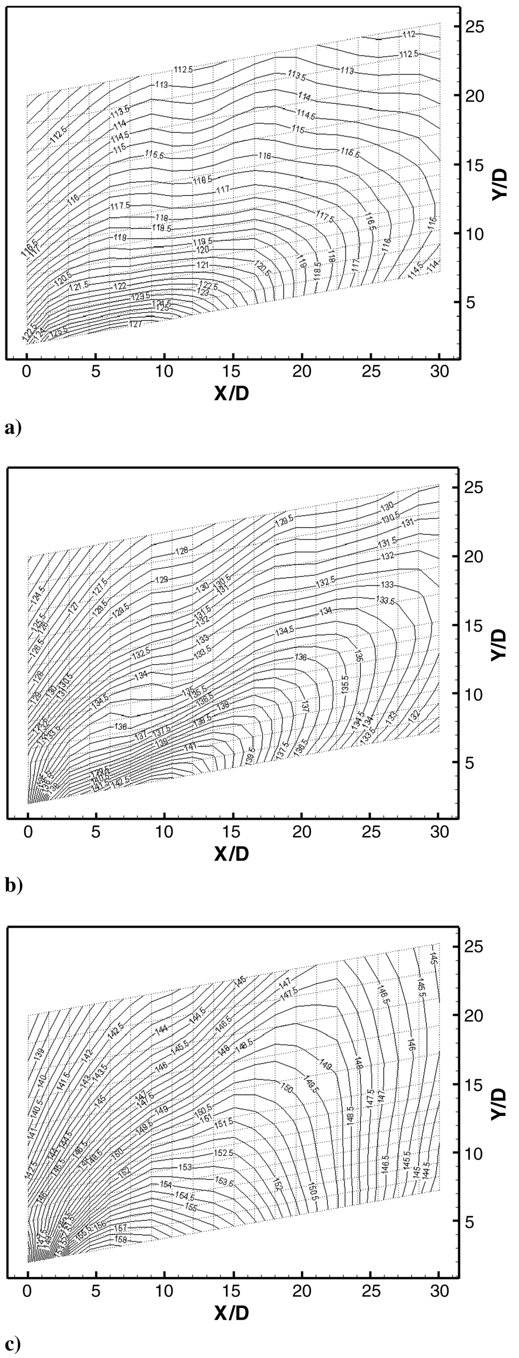

Fig. 29 Near-field contours of OASPL, $T_t/T_a = 3.2$: a) $M_j = 0.51$, b) $M_j = 0.90$, and c) $M_j = 1.67$.

source characteristics. The near-field contours of OASPL for three heated jets with $T_t/T_a = 3.2$ and Mach numbers of 0.51, 0.9, and 1.67 are presented in Fig. 29. Good similarity of closed lobes with preferential radiation of noise to the aft angles is observed for all the cases. The shift in peak radiation angle to a lower inlet angle for the heated $M_j = 1.67$ is evident.

The far-field spectra from jets at various test conditions have been examined. The spectral peak in the far field, at the maximum radiation angle of ∼150°, occurs at a Strouhal number in the range of ∼0.18 to ∼0.23. Selected contours in this Strouhal number range for two jets with $M_j = 1.67$ and $T_t/T_a = 1.0$ ($St = 0.19$) and $M_j = 0.90$ and $T_t/T_a = 3.2$ ($St = 0.22$) are presented in Fig. 30. The convective Mach numbers for these two cases are 0.93 and 1.05, respectively. There are some wiggles and anomalies in the contours; these are caused by the plotting program, because of the coarse grid used for mapping, and should be recognized as such. There are closely spaced, almost parallel contour lines that emanate from the jet. Again, there are well-defined loops that point in the downstream direction. The significance of these loops, as being due to the growth, saturation, and decay of instability waves, is explained by Tam [49]. Tam showed that the near-field pattern of a high-speed jet obtained with an instability wave analysis closely matches the measured contours by Troutt and McLaughlin [8]. The observed trends for these high-speed jets are not surprising and are in agreement with past observations.

The near-field contours of four lower-speed jets are next examined in Fig. 31. The jet operating conditions and the Strouhal numbers are, respectively, 1) $M_j = 0.51$ and $T_t/T_a = 1.0$ ($St = 0.21$), 2) $M_j = 0.60$ and $T_t/T_a = 1.0$ ($St = 0.19$), 3) $M_j = 0.90$ and $T_t/T_a = 1.0$ ($St = 0.22$), and 4) $M_j = 0.51$ and $T_t/T_a = 3.2$ ($St = 0.20$). The corresponding convective Mach numbers are 0.36, 0.41, 0.58, and 0.64, respectively. Attention is drawn to several features:

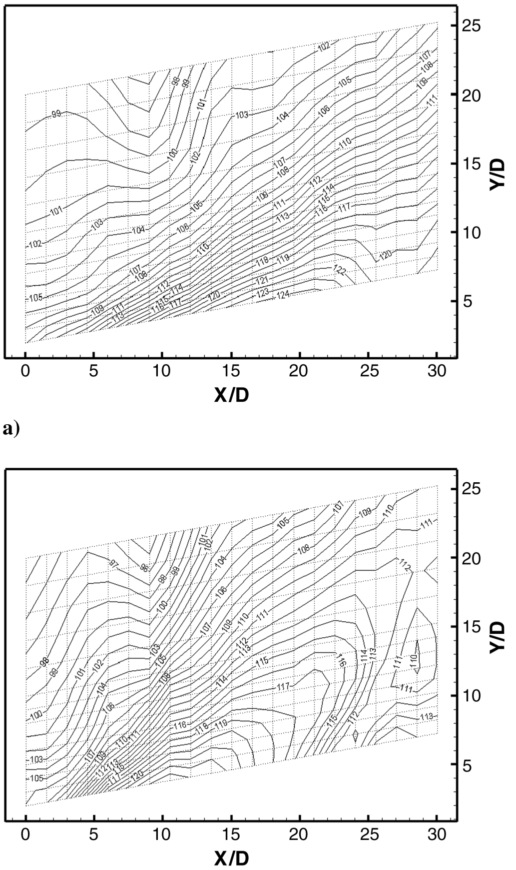

a)

b)

Fig. 30 Near-field contours at peak frequencies: a) $M_j = 1.67$ and $T_t/T_a = 1.0$ ($St = 0.19$) and b) $M_j = 0.90$ and $T_t/T_a = 3.2$ ($St = 0.22$).

1) The closed loops and preferential beaming to aft angles are seen for all four cases.

2) The orientation or the angle of the closed loops with respect to the jet axis increases with increasing M_c.

3) The axial extents of the highest contours in each plot, which are closest to the boundary of the jet, are quite long. The values of these are ∼8D for the 86 dB contour, ∼8D for the 92 dB contour, ∼12D for the 102 dB contour, and ∼9D for the 108 dB contour, respectively.

4) The source regions that radiate at the peak frequency and to the peak angle are coherent over many diameters and are not localized sources.

These features are similar to those seen for the high-speed jets in Fig. 29. Thus, the near-field characteristics are very similar for all jet velocities.

Sample near-field contours at a much higher frequency of 40 kHz are shown in Fig. 32. The jet conditions are, respectively, 1) $M_j = 0.51$ and $T_t/T_a = 1.0$ ($St = 14.28$), 2) $M_j = 0.51$ and $T_t/T_a = 3.2$ ($St = 7.95$), 3) $M_j = 0.90$ and $T_t/T_a = 3.2$ ($St= 4.84$), and 4) $M_j = 1.67$ and $T_t/T_a = 3.2$ ($St = 3.0$). The convective Mach numbers for these cases are 0.36, 0.64, 1.05, and 1.69, respectively. There are striking differences between these contours and those shown in Fig. 30. First of all, these high-frequency sources are located closer to the nozzle exit; secondly, these sources are localized and do not have the extended axial range as seen for the peak frequency. These near-field contours are consistent with the results presented in Secs. III.C and III.D.

F. Far-Field–Far-Field Correlations

Viswanathan [45,46] presented far-field–far-field correlations and identified several characteristics. Two sample plots from these studies are included here for the sake of completeness and for bringing together all aspects of near-field and far-field correlations. First, we present the correlations for a heated jet: $M_j = 0.9$, $T_t/T_a= 3.2$, and $M_c = 1.05$, with supersonic convective Mach number. Figure 33 shows polar correlations, for two different reference microphones at 150 and 90°, respectively. As the separation angle between the reference (fixed) and the second microphone is increased, the value of the maximum correlation coefficient decreases progressively. For the 150° microphone, there is high correlation for an extended angular range; the coefficient drops to ∼0.2 (20%) at an angle of 125°. The trend is very different for the 90° microphone; the correlation drops to ∼0.2 (20%) when the polar separation angle is only ±10°. The correlation functions in the azimuthal plane for the two polar angles of 150 and 90° are shown in Fig. 11 in [45]. Where a high-correlation level of ∼0.65 (65%) is maintained for a separation angle of 150° in the peak radiation direction, the levels fall below 0.20 for a separation angle of 40° at the forward angles. Comparable high azimuthal correlation levels, ≥ 0.54 for microphones separated by 150°, are observed at large aft angles for a very low-velocity jet with $M_j = 0.4$, $T_t/T_a = 1.0$, and $M_c = 0.28$ (see Fig. 12 in [45]).

The variation of the peak polar correlation with separation angle for a range of low to high jet velocities is examined. The reference microphone is at the peak radiation angle of 150°. Figure 34 shows such a variation for four test cases: unheated jets with $M = 0.4$ and 0.5 and two $M = 0.9$ jets with stagnation temperature ratios of 2.7 and 3.2. The corresponding V_j/a are 0.4, 0.49, 1.38, and 1.5, respectively. There are remarkable similarities in the trends for all the jets, in spite of the vast disparity in the jet velocities. The peak correlation values are slightly higher for the high-speed jets, but not by a significant amount; high-correlation levels of ∼0.18 persist down to an angle of 125°. The reason for the observed similarity is explained in detail in Sec. III of Tam et al. [50]. The key idea is that the width of the acoustic beam in the peak radiation direction is of the order of the size of the coherent source, thereby increasing the probability of two microphones located in the peak radiation sector measuring the same pulse and consequently leading to a high-correlation level. If this is the underlying physics, then the intensity of sound would play only a lesser role. The preceding hypothesis of Tam et al. [50] is validated by the trends seen in Fig. 34, as the peak correlation levels are comparable for low- and high-speed jets and are

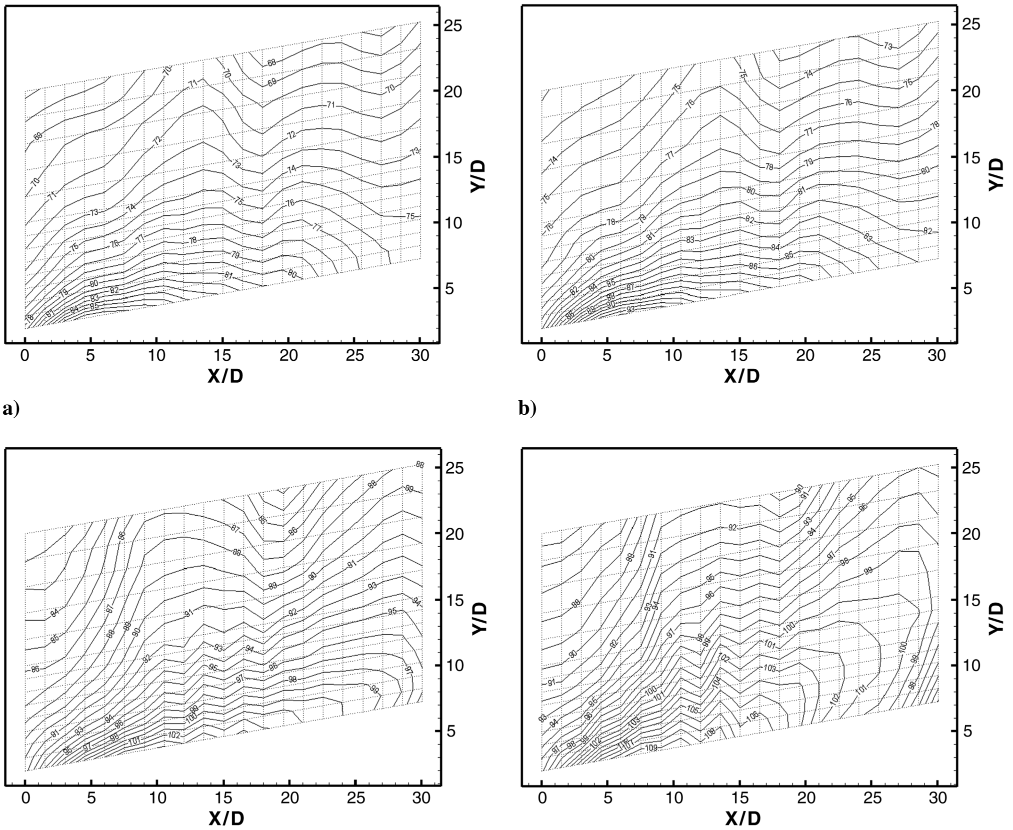

a) b) c) d)

Fig. 31 Near-field contours at peak frequencies: a) $M_j = 0.51$ and $T_t/T_a = 1.0$ ($St = 0.21$), b) $M_j = 0.60$ and $T_t/T_a = 1.0$ ($St = 0.19$), c) $M_j = 0.90$ and $T_t/T_a = 1.0$ ($St = 0.22$), and d) $M_j = 0.51$ and $T_t/T_a = 3.2$ ($St = 0.20$).

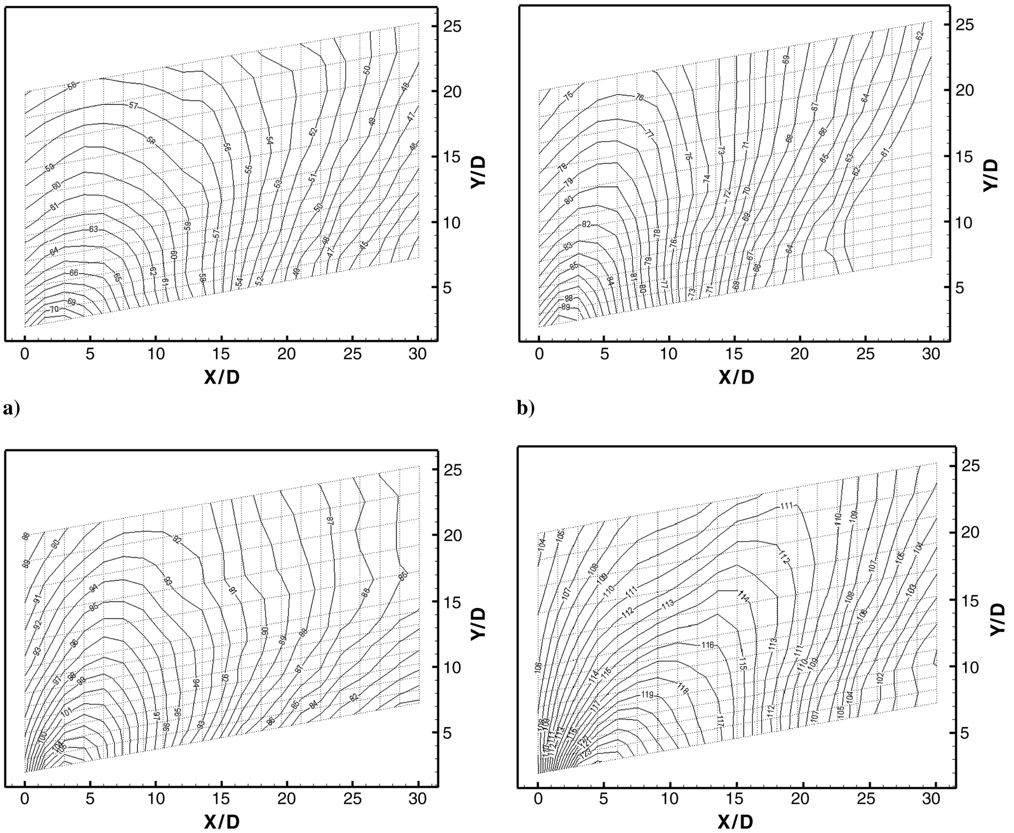

a) b) c) d)

Fig. 32 Near-field contours at high frequency of 40 kHz: a) $M_j = 0.51$ and $T_t/T_a = 1.0$, b) $M_j = 0.51$ and $T_t/T_a = 3.2$, c) $M_j = 0.90$ and $T_t/T_a = 3.2$, and 4) $M_j = 1.67$ and $T_t/T_a = 3.2$.

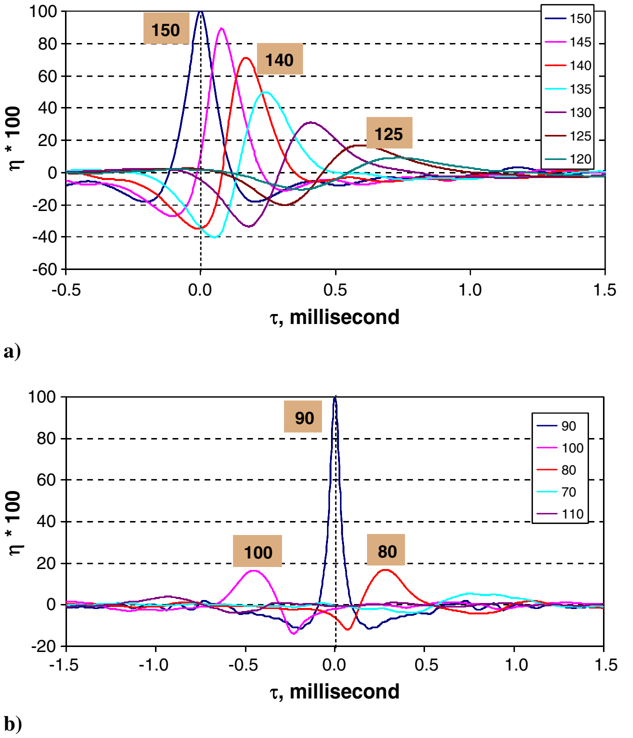

Fig. 33 Polar correlations, $M_j = 0.90$ and $T_t/T_a = 3.2$: a) reference microphone at 150° and b) reference microphone at 90°.

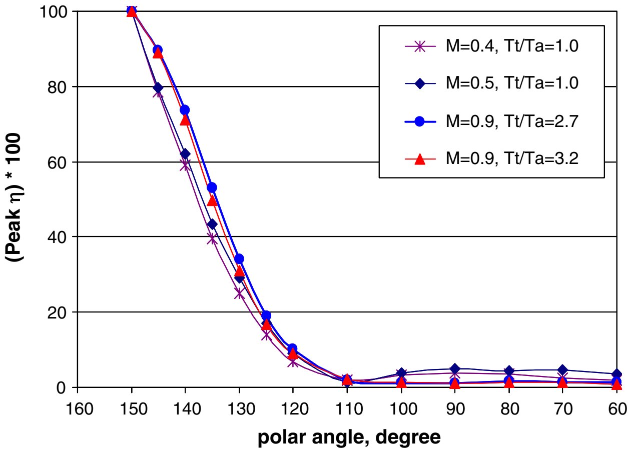

Fig. 34 Variation of the peak correlation with angle; reference microphone at 150°.

seen to be relatively independent of sound amplitude. The trends seen in Fig. 34, taken together with the results presented in Secs. III.C–III.E, suggest strongly that the mechanism by which the coherent source generates noise could be the same for jets at different velocities, from very low to supersonically convective. The evidence presented so far also indicates that the noise radiated to lower angles, $\leq \sim 110°$, is not from the coherent source. The random fine-scale turbulence is most likely the dominant source radiating to these directions.

IV. Conclusions

The space–time correlation characteristics of jets operated over a wide range of jet velocities have been investigated in this study, in order to gain a better understanding of the sources of jet noise. A traversing semicircular cage array, which spans 180° in the azimuthal direction, is specifically designed and built. The axial extent of the cage array is $30D$. Four different far-field microphone arrays are also deployed, to obtain a comprehensive picture of the near and far acoustic fields. A convergent nozzle and a CD nozzle with a design Mach number of 1.67 are used. Unheated jets and heated jets at a stagnation temperature ratio T_t/T_a of 3.2 over a wide range of jet Mach numbers from 0.51 to 1.67 have been considered. The convective Mach number M_c, taken to be $0.7(V_j/a)$, spans a range of 0.36 to 1.69. The lack of acoustic interference of the cage array has been demonstrated through good agreement of far-field spectra taken with and without the presence of the cage array. The many steps taken to minimize/eliminate reflections from the cage array turned out to be efficacious.

First, the following are established through a recap of source measurements with an elliptic mirror:

1) The peak overall source locations are located well beyond the end of the potential core from the nozzle exit plane.

2) The low-frequency sources are not localized but extend to $\sim 20D$ in the axial direction.

These results provided critical information in the design and choice of the length for the cage array: at least $30D$. The main conclusions from the near-field space–time correlations are as follows:

1) There is very little axial correlation when the reference microphone is close to the nozzle exit, in the range of $x/D = 1$ to ~ 7; definite trends begin to emerge when the reference microphone is located at $x/D \geq \sim 10.5$.

2) There is a large region of highly coherent pressure fluctuations that extends over $\sim 15D$ axially and $\sim 360°$ azimuthally for all jet conditions, from $M_c = 0.36$ to 1.69.

3) The coherent region typically extends from $\sim 13D$ to $\sim 31D$, with maximum normalized correlation levels greater than ~ 0.5 (50%) over the entire axial extent of $\sim 15D$.

4) These high levels of normalized correlations are observed at all jet velocities, from $M_c = 0.36$ to 1.69.

The peak pressure occurs between $\sim 6D$ to $\sim 8D$ for the range of Mach numbers considered; thus, the peak pressure location is observed close to the end of the potential core for each jet. However, the large coherent source extends from $\sim 13D$ to $\sim 31D$, well beyond twice the length of the potential core. This is a new finding and has not been reported in any prior study. The results from the near-field and elliptic mirror measurements are consistent and mutually supporting. These observations lend evidence to the premise that the features of the true acoustic sources would be imprinted on the near-field pressure correlations. Therefore, there is reason to believe that the large region of highly coherent pressure fluctuations represents an equivalent source.

From the near-field–far-field correlations, the following characteristics are established:

1) There is no measurable correlation, taken to be $\leq \sim 0.1$ (10%), for inlet angles $\leq \sim 110°$ for any jet condition tested and for any location in the near field of the jet: the dominant source radiating to these angles is most likely the random fine-scale turbulence.

2) There is a clear difference in the variation of the peak near-field–far-field correlation for heated and unheated jets: there is no discernible correlation for the angular range of 120° to $\sim 130°$ for unheated jets with $M_j = 0.51$ to 1.67, whereas there are good peak correlation levels of ~ 0.60 to ~ 0.35 for the $M_j = 0.51$ to 1.67 heated jets with $T_t/T_a = 3.2$.

3) The axial locations in the near field for these peak correlations in the angular range of 120 to $\sim 130°$ occur closer to the nozzle exit than those for large aft angles.

4) There is an extended axial range of $\sim 15D$ where high correlations of ~ 0.5 (50%) to ~ 0.8 (80%) are observed between a single point in the near-field and the far-field microphone signal at 150°. These high levels of peak correlations are seen for jets at all jet velocities, from $M_c = 0.36$ to 1.69.

The near-field maps of the pressure contours, on which the source characteristics are imprinted, corroborate the trends seen with both the near-field space–time features and the near-field–far-field correlations. The source characteristics responsible for the peak spectral level in the far field are coherent over an extended axial range and are similar for jets over the entire range of jet velocities considered in this study. Closed loops and preferred orientations of the lobes to large aft angles attest to the coherent nature of the source.

Finally, the far-field–far-field correlations both for low-speed and high-speed jets exhibit remarkable similarity. There is high polar correlation, over an angular range of ∼25°, when the reference microphone is located at 150°. However, there is virtually no correlation when the reference microphone is at 90°. The variations of the maximum correlations, for the reference microphone located at 150°, are almost identical for low-and high-speed jets. The various results are consistent and denote the role of the coherent source in the radiation of noise to the peak angle. Further, the jet velocity is seen to have minor, if any, effect on the measured characteristics. Thus, there seems to be a single mechanism/source responsible for the generation and radiation of noise to the peak radiation sector. This hypothesis was put forward by Viswanathan [45,46], based on the analyses of far-field measurements alone. The comprehensive set of measurements, both in the near field and far field, has bolstered this statement and has provided fresh additional evidence.

Acknowledgments

It is a pleasure to thank Guy Neubert for processing the time-series data and the Boeing Low-Speed Aeroacoustics Facility test crew for setting up and operating the microphone array. The design for the shock-free convergent–divergent nozzle was provided by James Bridges and Nick Georgiadis of NASA John H. Glenn Research Center at Lewis Field; their help is gratefully acknowledged.

References

[1] Maestrello, L., "On the Relationship Between Acoustic Energy Density Flux near the Jet Axis and Far-Field Acoustic Intensity," NASA TN D-7269, Oct. 1973.

[2] Siddon, T. E., "Noise Source Diagnostics Using Causality Relations," AGARD CP-131, 1974, pp. 7.1–7.13.

[3] Seiner, J. M., and Reethof, G., "On the Distribution of Source Coherency in Subsonic Jets," AIAA Paper 1974-4, 1974.

[4] McLaughlin, D. K., Morrison, G. L., and Troutt, T. R., "Experiments on the Instability Waves in a Supersonic Jet and Their Acoustic Radiation," *Journal of Fluid Mechanics*, Vol. 69, No. 1, 1975, pp. 73–85. doi:10.1017/S0022112075001322

[5] Ribner, H. S., "Two-Point Correlations of Jet Noise," *Journal of Sound and Vibration*, Vol. 56, No. 1, 1978, pp. 1–19. doi:10.1016/0022-460X(78)90566-7

[6] Schaffar, M., "Direct Measurements of the Correlation Between Axial In-Jet Velocity Fluctuations and Far Field Noise near the Axis of a Cold Jet," *Journal of Sound and Vibration*, Vol. 64, No. 1, 1979, pp. 73–83. doi:10.1016/0022-460X(79)90573-X

[7] Richarz, W. G., "Direct Correlation of Noise and Flow of a Jet Using Laser Doppler," *AIAA Journal*, Vol. 18, No. 7, 1980, pp. 759–765. doi:10.2514/3.50817

[8] Troutt, T. R., and McLaughlin, D. K., "Experiments on the Flow and Acoustic Properties of a Moderate-Reynolds-Number Supersonic Jet," *Journal of Fluid Mechanics*, Vol. 116, No. 1, 1982, pp. 123–156. doi:10.1017/S0022112082000408

[9] Seasholtz, R. G., Panda, J., and Elam, K. A., "Rayleigh Scattering Diagnostics for Measurement of Velocity and Density Fluctuation Spectra," AIAA Paper 2002-0827, 2002.

[10] Panda, J., and Seasholtz, R. G., "Experimental Investigation of Density Fluctuations in High-Speed Jets and Correlation with Generated Noise," *Journal of Fluid Mechanics*, Vol. 450, 2002, pp. 97–130.

[11] Panda, J., Seasholtz, R. G., and Elam, K. A., "Investigation of Noise Sources in High-Speed Jets via Correlation Measurements," *Journal of Fluid Mechanics*, Vol. 537, No. 1, 2005, pp. 349–385. doi:10.1017/S0022112005005148

[12] Bridges, J., and Wernet, M. P., "Measurements of the Aeroacoustic Sound Source in Hot Jets," Ninth AIAA/CEAS Aeroacoustics Conference, AIAA/CEAS Paper 2003-3130, May 2003.

[13] Bridges, J., "Effect of Heat on Space–Time Correlations in Jets," 12th AIAA/CEAS Aeroacoustics Conference, AIAA/CEAS Paper 2006-2534, May 2006.

[14] Bridges, J., and Wernet, M. P., "Effect of Temperature on Jet Velocity Spectra," 13th AIAA/CEAS Aeroacoustics Conference, AIAA/CEAS Paper 2007-3628, May 2007.

[15] Fleury, V., Bailley, C., Jondeau, E., Michard, M., and Juvé, D., "Space–Time Correlations in Two Subsonic Jets Using Dual Particle Image Velocimetry Measurements," *AIAA Journal*, Vol. 46, No. 10, Oct. 2008, pp. 2498–2509. doi:10.2514/1.35561

[16] Suzuki, T., and Colonius, T., "Instability Waves in a Subsonic Detected Using a Near-Field Phased Microphone Array," *Journal of Fluid Mechanics*, Vol. 565, 2006, pp. 197–226. doi:10.1017/S0022112006001613

[17] Ukeiley, L. S., and Ponton, M. K., "On the Near Field Pressure of a Transonic Axisymmetric Jet," *International Journal of Aeroacoustics*, Vol. 3, No. 1, 2004, pp. 43–66. doi:10.1260/1475472043 23022257

[18] Arndt, R. E. A., Long, D. F., and Glauser, M. N., "The Proper Orthogonal Decomposition of Pressure Fluctuations Surrounding a Turbulent Jet," *Journal of Fluid Mechanics*, Vol. 340, 1997, pp. 1–33. doi:10.1017/S0022112097005089

[19] Reba, R. A., Narayanan, S., Colonius, T., and Suzuki, T., "Modeling Jet Noise from Organized Structures Using Near-Field Hydrodynamic Pressure," 11th AIAA/CEAS Aeroacoustics Conference, AIAA/CEAS Paper 2005-3093, May 2005.

[20] Reba, R. A., Simonich, J. C., and Schlinker, R. H., "Measurement of Source Wave-Packets in High-Speed Jets and Connection to Far-Field Sound," 14th AIAA/CEAS Aeroacoustics Conference, AIAA/CEAS Paper 2008-2891, May 2008.

[21] Reba, R. A., Simonich, J. C., and Schlinker, R. H., "Sound Radiated by Large-Scale Wave-Packets in Subsonic and Supersonic Jets," 15th AIAA/CEAS Aeroacoustics Conference, AIAA/CEAS Paper 2009-3256, May 2009.

[22] Ladeinde, F., Cai, X., Alabi, K., Reba, R. A., Schlinker, R. H., and Simonich, J. C., "On the Connection Between Near-Field and Far-Field Solutions of High-Speed Jet Noise," 46th Aerospace Sciences Meeting, AIAA Paper 2008-11, Reno, NV, Jan. 2006.

[23] Hileman, J., Thurow, B., and Samimy, M., "Exploring Noise Sources Using Simultaneous Acoustic Measurements and Real-Time Flow Visualization in Jets," *AIAA Journal*, Vol. 40, No. 12, 2002, pp. 2382–2392. doi:10.2514/2.1599

[24] Hileman, J., Carballo, E., Thurow, B., and Samimy, M., "Large-Scale Structure Evolution and Sound Emission in High-Speed Jets: Real-Time Visualization with Simultaneous Acoustic Measurements," *Journal of Fluid Mechanics*, Vol. 544, No. 1, 2005, pp. 277–307. doi:10.1017/S002211200500666X

[25] Power, O., Kerhervé, F., Fitzpatrick, J., and Jordan, P., "Measurements of Turbulence Statistics in High Subsonic Jets," 10th AIAA/CEAS Aeroacoustics Conference, AIAA/CEAS Paper 2004-3021, May 2004.

[26] Tinney, C. E., Jordan, P., Delville, J., Hall, A. M., and Glauser, M. N., "A Time-Resolved Estimate of the Turbulence and Source Mechanisms in a Subsonic Jet Flow," 44th Aerospace Sciences Meeting, AIAA Paper 2006-621, Reno, NV, Jan. 2006.

[27] George, W. K., Wänström, M., and Jordan, P., "Identifying Aeroacoustic Sources," 13th AIAA/CEAS Aeroacoustics Conference, AIAA/CEAS Paper 2007-3603, May 2007.

[28] Laurendeau, E., Jordan, P., Delville, J., and Bonnet, J. P., "Near-Field–Far-Field Correlations in Subsonic Jets: What Can They Tell Us?," 13th AIAA/CEAS Aeroacoustics Conference, AIAA/CEAS Paper 2007-3614, May 2007.

[29] Guitton, A., Kerhervé, F., Jordan, P., and Delville, J., "The Sound Production Mechanism Associated with Coherent Structures in Subsonic Jets," 14th AIAA/CEAS Aeroacoustics Conference, AIAA/CEAS Paper 2008-2892, May 2008.

[30] Jordan, P., Coiffet, F., Delville, J., and Gervais, Y., "Acoustic-Hydrodynamic Interaction in the Entrainment Region of Subsonic Jet Flow," 10th AIAA/CEAS Aeroacoustics Conference, AIAA/CEAS Paper 2004-3020, May 2004.

[31] Doty, M. J., and McLaughlin, D. K., "Space–Time Correlation Measurements of High-Speed Axisymmetric Jets Using Optical Deflectometry," *Experiments in Fluids*, Vol. 38, No. 25, 2004, pp. 415–425.

[32] Petitjean, B., Viswanathan, K., McLaughlin, D. K., and Morris, P. J., "Space–Time Correlation Measurements in Subsonic and Supersonic Jets Using Optical Deflectometry," 13th AIAA/CEAS Aeroacoustics Conference, AIAA/CEAS Paper 2007-3613, May 2007.

[33] Papamoschou, D., Morris, P. J., and McLaughlin, D. K., "Beamformed Flow-Acoustic Correlations in High-Speed Jets," 15th AIAA/CEAS Aeroacoustics Conference, AIAA/CEAS Paper 2009-3212, May 2009.

[34] Bogey, C., Barré, S., Fleury, V., Bailley, C., and Juvé, D., "Experimental Study of the Spectral Properties of Near-Field and Far-Field Jet Noise," *International Journal of Aeroacoustics*, Vol. 6, No. 2, 2007, pp. 73–92.

doi:10.1260/147547207781041868

[35] Callender, B., Gutmark, E., and Martens, S., "Near-Field Investigation of Chevron Nozzle Mechanisms," *AIAA Journal*, Vol. 46, No. 1, 2008, pp. 36–45.
doi:10.2514/1.17720

[36] Kastner, J., Cuppoletti, D., Gutmark, G., Fahrland, A., Jeffries, J., and Hanson, R., "Simultaneous Measurement of Flow Fluctuations and Near-Field Pressure in a Subsonic Jet," 15th AIAA/CEAS Aeroacoustics Conference, AIAA/CEAS Paper 2009-3211, May 2009.

[37] Viswanathan, K., "Distributions of Noise Sources in Heated and Cold Jets: Are They Different?" *International Journal of Aeroacoustics*, Vol. 9, Nos. 4–5, 2010, pp. 589–625.
doi:10.1260/1475-472X.9.4-5.589

[38] Tam, C., Pastouchenko, N., and Viswanathan, K., "Continuation of the Near Acoustic Field of a Jet to the Far Field. Part 1: Theory," AIAA/CEAS Paper 2010-3728, June 2010.

[39] Tam, C., Viswanathan, K., Pastouchenko, N., and Tam, B., "Continuation of the Near Acoustic Field of a Jet to the Far Field. Part 2: Experimental Validation and Noise Source Characteristics," AIAA/CEAS Paper 2010-3729, June 2010.

[40] Viswanathan, K., "Jet Aeroacoustic Testing: Issues and Implications," *AIAA Journal*, Vol. 41, No. 9, 2003, pp. 1674–1689.
doi:10.2514/2.7313

[41] Viswanathan, K., "Aeroacoustics of Hot Jets," *Journal of Fluid Mechanics*, Vol. 516, 2004, pp. 39–82.
doi:10.1017/S0022112004000151

[42] Viswanathan, K., "Instrumentation Considerations for Accurate Jet Noise Measurements," *AIAA Journal*, Vol. 44, No. 6, 2006, pp. 1137–1149.
doi:10.2514/1.13518

[43] Underbrink, J. R., "Hardware Architecture and Applications for a Distributed, High Bandwidth, High Channel Count Acoustic Data Acquisition System," NIWeek 2007 Sound and Vibration Summit, Austin, TX, 2007.

[44] Underbrink, J. R., "Software Architecture for a Distributed, High Bandwidth, High Channel Count Acoustic Data Acquisition System," NIWeek 2007 Sound and Vibration Summit, Austin, TX, 2007.

[45] Viswanathan, K., "Investigation of Noise Source Mechanisms in Subsonic Jets," *AIAA Journal*, Vol. 46, No. 8, Aug. 2008, pp. 2020–2032.
doi:10.2514/1.34471

[46] Viswanathan, K., "Mechanisms of Jet Noise Generation: Classical Theories and Recent Developments," *International Journal of Aeroacoustics*, Vol. 8, No. 4, 2009, pp. 355–408.
doi:10.1260/147547209787548949

[47] Witze, P. O., "Centerline Velocity Decay of Compressible Free Jets," *AIAA Journal*, Vol. 12, No. 4, 1974, pp. 417–418.
doi:10.2514/3.49262

[48] Lau, J. C., "Effects of Exit Mach Number and Temperature on Mean-Flow and Turbulence Characteristics in Round Jets," *Journal of Fluid Mechanics*, Vol. 105, No. 1, 1981, pp. 193–218.
doi:10.1017/S0022112081003170

[49] Tam, C. K. W., "Mach Wave Radiation from High-Speed Jets," *AIAA Journal*, Vol. 47, No. 10, Oct. 2009, pp. 2440–2448.
doi:10.2514/1.42644

[50] Tam, C. K. W., Viswanathan, K., Ahuja, K. K., and Panda, J., "The Sources of Jet Noise: Experimental Evidence," *Journal of Fluid Mechanics*, Vol. 615, 2008, pp. 253–292.
doi:10.1017/S0022112008003704

A. Lyrintzis
Associate Editor